Systematic global structure search of bismuth-based binary systems under pressure using machine learning potentials

Hayato Wakai,[1,*] Shintaro Ishiwata,[2,3] and Atsuto Seko[1,†]

[1] *Department of Materials Science and Engineering, Kyoto University, Kyoto 606-8501, Japan*
[2] *Division of Materials Physics and Center for Spintronics Research Network (CSRN), Graduate School of Engineering Science, The University of Osaka, Toyonaka, Osaka 560-8531, Japan*
[3] *Spintronics Research Network Division, Institute for Open and Transdisciplinary Research Initiatives, The University of Osaka, Suita, Osaka 565-0871, Japan*

(Dated: November 10, 2025)

Machine learning potentials (MLPs) have significantly advanced global crystal structure prediction by enabling efficient and accurate property evaluations. In this study, global structure searches are performed for 11 bismuth-based binary systems, including Na–Bi, Ca–Bi, and Eu–Bi, under pressures ranging from 0 to 20 GPa, employing polynomial MLPs developed specifically for these systems. The searches reveal numerous compounds not previously reported in the literature and identify all experimentally known compounds that are representable within the explored configurational space. These results highlight the robustness and reliability of the current MLP-based structure search. The study provides valuable insights into the discovery and design of novel bismuth-based materials under both ambient and high-pressure conditions.

I. INTRODUCTION

Machine learning potentials (MLPs) have become a key tool for enabling accurate large-scale atomistic simulations and extensive repeated calculations. MLPs can flexibly represent short-range interatomic interactions by employing a variety of structural features that characterize the local atomic environment, in conjunction with machine learning models such as artificial neural networks [1–9], Gaussian processes [10–14], and linear models [15–21]. Although these MLP models include numerous coefficients, they are estimated using datasets generated from extensive density functional theory (DFT) calculations. Depending on the structural diversity of the DFT dataset, MLPs can be developed to either exhibit broad predictive power across a wide range of atomic configurations or to be highly specialized for a specific target structure.

Global crystal structure searches based on DFT calculations have become a powerful approach for predicting globally stable and metastable structures over a wide range of pressures [22–25]. Replacing DFT calculations with those using MLPs that exhibit high predictive power across diverse structures can be considered a straightforward strategy to accelerate global structure searches. However, several technical challenges remain in integrating MLPs with global structure search methods. Recently, significant acceleration of global structure searches using MLPs has been demonstrated by enabling efficient and accurate evaluation of energies and forces during local geometry optimizations [26–31]. The integration of MLPs enables efficient exploration of vast configurational spaces that would otherwise be computationally infeasible with DFT alone, thereby substantially improving the reliability of identifying the true global minimum structures.

Thanks to the efficiency of MLP-based global structure searches, they can now be systematically applied to a variety of systems and pressure conditions, which was previously almost impossible to achieve using only DFT calculations. By performing such high-throughput global structure searches, previously unknown stable compounds can be discovered, thereby accelerating the exploration and design of novel materials.

In this study, we systematically perform global structure searches, beginning with the development of MLPs, to discover previously unknown stable compounds in 11 bismuth-based binary systems within the pressure range of 0–20 GPa. Bismuth-containing compounds have attracted considerable attention due to their diverse electronic properties arising from the strong spin-orbit coupling of the heavy element bismuth, which plays a crucial role in the emergence of topologically nontrivial band structures. However, global structure searches using DFT calculations have so far been reported for only a limited number of systems and conditions [32, 33], in part because of the high computational cost associated with such searches.

We investigate bismuth-based binary X–Bi systems, where the element X is selected from distinct elemental groups: the alkali metals sodium and potassium; the alkaline earth metals magnesium, calcium, strontium, and barium; the group 3 metals scandium, yttrium, and lanthanum; and the rare-earth metals europium and gadolinium. Among the systems considered here, Na_3Bi is widely recognized as a topological Dirac semimetal [34], and K_3Bi has also been theoretically predicted to exhibit similar behavior [35]. Moreover, superconductivity has been reported in several Bi-based binary compounds, including NaBi, KBi_2, $Ca_{11}Bi_{10-x}$, $CaBi_2$, $SrBi_3$, Ba_2Bi_3, $BaBi_3$, YBi, LaBi, and $LaBi_3$ [36–45]. Additionally, ex-

* wakai@cms.mtl.kyoto-u.ac.jp
† seko@cms.mtl.kyoto-u.ac.jp

tremely large magnetoresistance has been observed in YBi, LaBi, and GdBi at low temperatures [43, 44, 46].

This study employs the polynomial MLP framework, in which interatomic interactions are represented by polynomial rotational invariants systematically derived from structural order parameters based on radial functions and spherical harmonics [20, 47, 48]. This study also adopts an approach that integrates a polynomial MLP with random structure search (RSS), which has been reported to achieve high predictive accuracy across a wide range of crystal structures. This approach has been applied to various systems, including the prediction of stable compounds in binary and ternary alloy systems [31, 49], the enumeration of globally stable and metastable structures in elemental systems exhibiting numerous local minima with energies close to the global minimum [50], and the construction of pressure–temperature phase diagrams through systematic anharmonic lattice dynamics calculations for both global and local minimum structures [51]. In this study, the same approach is applied to perform global structure searches in bismuth-based systems. As a result, the present structure searches not only reveal numerous previously unreported stable compounds under both ambient and high-pressure conditions, but also reproduce experimentally reported structures.

II. METHODOLOGY

A. MLP development

In this section, we describe the procedures for developing polynomial MLPs that enable robust and efficient global structure searches. We first construct an initial DFT dataset composed of structures randomly modified from various prototype structures. Based on this dataset, an initial MLP is then trained, as described in Sec. II A 2. Subsequently, RSS calculations are carried out using this initial MLP, as outlined in Sec. II A 3. Single-point DFT calculations are performed for the local minimum structures obtained from RSS, and their results are incorporated into the training dataset. The MLP is retrained on the expanded dataset, and RSS is repeated with the updated MLP. This iterative process of RSS and MLP retraining progressively enhances the predictive accuracy of the MLP for local minimum structures. As a result of this iterative procedure, a final MLP capable of accurate global structure searches is obtained.

1. *Formulation of the polynomial MLP*

We provide a brief overview of the polynomial MLP formulation applied to binary systems [47, 48]. As discussed in Refs. [20, 52], the polynomial MLPs can be regarded as a generalization of embedded atom method (EAM) potentials [53], modified EAM potentials [54], simple polynomial models with pair and angular features [15, 52, 55], a spectral neighbor analysis potential (SNAP) [16], and a quadratic SNAP [19]. Moreover, linear polynomial models constructed using polynomial invariants are analogous to the formulation of the atomic cluster expansion [21].

In the polynomial MLP, the short-range part of the potential energy for a structure, E, is assumed to be decomposed as $E = \sum_i E^{(i)}$, where $E^{(i)}$ denotes the contribution of interactions between atom i and its neighboring atoms within a given cutoff radius r_c, referred to as the atomic energy. The atomic energy is then approximately expressed in terms of the polynomial rotational invariants $\{d_m^{(i)}\}$, which are derived from order parameters, as

$$E^{(i)} = F\left(d_1^{(i)}, d_2^{(i)}, \cdots\right), \tag{1}$$

where the function F denotes a polynomial function. In this study, basis sets composed of radial functions $\{f_n\}$ and spherical harmonic functions $\{Y_{lm}\}$ are adopted to represent the neighboring atomic density. In this framework, the pth-order polynomial invariant for a given radial index n and a set of pairs $\{(l_1,t_1),(l_2,t_2),\ldots,(l_p,t_p)\}$, where each pair consists of the degree of the spherical harmonics l and an unordered element pair t, is defined as a linear combination of products of p order parameters, expressed as

$$\begin{aligned} &d^{(i)}_{nl_1l_2\cdots l_p,t_1t_2\cdots t_p,(\sigma)} \\ &= \sum_{m_1,m_2,\cdots,m_p} c^{l_1l_2\cdots l_p,(\sigma)}_{m_1m_2\cdots m_p} a^{(i)}_{nl_1m_1,t_1} a^{(i)}_{nl_2m_2,t_2}\cdots a^{(i)}_{nl_pm_p,t_p}, \end{aligned} \tag{2}$$

where the element pair t belongs to the set $\{\{\mathrm{A},\mathrm{A}\},\{\mathrm{A},\mathrm{B}\},\{\mathrm{B},\mathrm{B}\}\}$, with A and B representing distinct elements. $a^{(i)}_{nlm,t}$ denotes the order parameter for element unordered pair t of component nlm representing the partial neighboring atomic density around atom i. The coefficient set $\{c^{l_1l_2\cdots l_p,(\sigma)}_{m_1m_2\cdots m_p}\}$ ensures that the linear combinations are invariant for arbitrary rotations. When multiple invariants exist for a given set of $\{l\}$, they are distinguished by the index σ.

The current polynomial MLPs adopt a finite set of Gaussian-type radial functions modified by a cosine-based cutoff function to ensure smooth decay of the radial function [48]. The set of polynomial invariants $D^{(i)} = \{d_1^{(i)}, d_2^{(i)}, \cdots\}$ is generated based on input parameters, such as the cutoff radius, the number of radial functions, and the truncation of polynomial invariants. Given a set of polynomial invariants $D^{(i)}$, the polynomial function F_ξ composed of all combinations of ξ polynomial invariants is represented as

$$\begin{aligned} F_1\left(D^{(i)}\right) &= \sum_s w_s d_s^{(i)} \\ F_2\left(D^{(i)}\right) &= \sum_{\{st\}} w_{st} d_s^{(i)} d_t^{(i)}, \end{aligned} \tag{3}$$

where w denotes a regression coefficient. The atomic energy is then described by a polynomial of the polynomial invariants $D^{(i)}$ as

$$E^{(i)} = F_1\left(D^{(i)}\right) + F_2\left(D^{(i)}\right) + \cdots . \tag{4}$$

In addition to the model defined in Eq. (4), we also consider simpler models consisting of a linear polynomial of polynomial invariants and a polynomial of a subset of these polynomial invariants, as expressed by

$$E^{(i)} = F_1\left(D^{(i)}\right) + F_2\left(D^{(i)}_{\text{pair}} \cup D^{(i)}_2\right), \tag{5}$$

where the subsets of $D^{(i)}$ are defined as

$$D^{(i)}_{\text{pair}} = \{d^{(i)}_{n0}\}, D^{(i)}_2 = \{d^{(i)}_{nll}\}. \tag{6}$$

2. Development of initial MLP

For each binary system, we begin by constructing a dataset for developing an initial MLP, following the procedure that has been demonstrated to be effective not only for performing global structure searches [31, 49–51] but also for achieving high predictive accuracy across a broad range of crystalline systems [47], defective structures [56, 57], and liquid-state simulations [58]. The procedure for constructing the initial dataset is as follows. First, the atomic positions and lattice parameters of prototype structures are optimized using DFT calculations at 0 and 20 GPa. These prototypes cover a wide variety of structural types, including 86 prototype structures for the endmembers [20] and 150 prototype structures for binary compositions [47], which are selected from the Inorganic Crystal Structure Database (ICSD) [59]. Next, random structures are generated by introducing random lattice expansions, lattice distortions, and atomic displacements to the optimized prototype structures. Details of the random structure generation settings are provided in Appendix A. Single-point DFT calculations are then performed for these structures. As a result, each DFT dataset contains approximately 20,000–23,000 structures for each binary system. For MLP training, the DFT dataset is randomly divided into training and test sets, with 90% used for training and 10% for testing.

An initial MLP is then developed using the initial training and test datasets. Since polynomial MLPs inherently exhibit a trade-off between predictive accuracy and computational efficiency [20], we conduct a grid search to identify a set of Pareto-optimal models that offer different balances between these two factors. For each binary system, a total of 305 polynomial MLP models are evaluated. From the resulting Pareto-optimal set, one model is selected as the initial MLP based on an optimal compromise between accuracy and computational cost.

In these polynomial MLPs, the cutoff radius ranges from 6 to 10 Å, and the number of polynomial invariants spans from 260 to 108,800. The regression coefficients of the potential energy models are estimated using linear ridge regression, where the total energy, atomic forces, and stress tensors from the training dataset serve as the regression observations. Details of the MLP fitting procedure, including the governing equations and the data weighting strategy, are provided in Appendix B. Despite the training dataset containing over 850,000 entries, linear ridge regression enables efficient model training even with such a large dataset and high-dimensional feature space. All polynomial MLPs used in the grid search are developed using the PYPOLYMLP code [48, 60].

3. MLP update

To develop an MLP capable of performing robust global structure searches, the coefficients of the selected MLP model are iteratively updated from their initial values by incorporating DFT results for local minimum structures obtained through RSS into the training dataset. In this study, the MLP is updated through two successive iterations. During the RSS in the first iteration, the maximum number of atoms per unit cell is limited to 8, whereas in the second iteration, this limit is increased to 16. These structural searches are carried out at five discrete pressure points ranging from 0 to 20 GPa, with an interval of 5 GPa. A total of 220,000 and 760,000 initial random structures are generated in the first and second iterations, respectively. In the first iteration, all distinct local minima identified by RSS are added to the training dataset. In contrast, in the second iteration, only structures with enthalpy values close to the lowest at each composition are included, due to the large number of local minima obtained. Across the 11 binary systems, the total number of local minimum structures incorporated into the initial dataset ranges from approximately 28,000 to 43,000. By substantially expanding the initial dataset with structurally diverse candidates, we are able to develop accurate MLPs suitable for robust global structure searches.

4. Computational details of DFT calculations

Non-spin polarized DFT calculations were carried out using the plane-wave-basis projector augmented wave (PAW) method [61, 62] within the Perdew–Burke–Ernzerhof exchange-correlation functional [63] as implemented in the VASP code [64–66]. Based on convergence tests performed for several prototype structures, the cutoff energy was set to 400 eV, except for the La–Bi system, for which it was set to 330 eV. The spacing between k-points was approximately 0.09 Å^{-1}. At these cutoff energies and k-point grids, the total energies were found to be sufficiently converged. The total energies were converged to less than 10^{-3} meV per cell. The atomic positions and lattice constants of the prototype structures

were optimized until the residual forces were less than 10^{-2} eV/Å.

The configurations of the valence electrons in the PAW potentials are $2p^6 3s^1$ for Na, $3s^2$ for Mg, $3s^2 3p^6 4s^1$ for K, $3s^2 3p^6 4s^2$ for Ca, $3d^2 4s^1$ for Sc, $4s^2 4p^6 5s^2$ for Sr, $4s^2 4p^6 4d^2 5s^1$ for Y, $5s^2 5p^6 6s^2$ for Ba, $5s^2 5p^6 5d^1 6s^2$ for La, $5p^6 6s^2$ for Eu, $5p^6 5d^1 6s^2$ for Gd, and $6s^2 6p^3$ for Bi. These PAW potentials include scalar-relativistic corrections, and spin-orbit coupling was not explicitly considered in all systems. Note that we used the PAW potentials for Eu and Gd, in which $4f$ and $5s$ electrons are treated as core states. The supplemental material provides a comparison of the density of states calculated using these PAW potentials and other PAW potentials in which the $4f$ and $5s$ electrons are treated as valence states.

B. Global structure search

1. Random structure search

We employ RSS to enumerate globally stable and metastable structures, which corresponds to the multi-start method in global optimization [67]. In this approach, local geometry optimizations are repeatedly performed on randomly generated initial structures with diverse compositions. Compounds corresponding to local minimum structures that lie on the convex hull of the formation enthalpy are then considered thermodynamically stable. Although RSS is a simple approach that requires minimal parameter tuning, it effectively enumerates both global and local minimum structures through unbiased sampling of a broad configurational space. Furthermore, the method can be performed efficiently owing to its ease of parallelization. This heuristic approach has been widely adopted, notably within the *ab initio* random structure search (AIRSS) framework [23, 68–70]. In the present study, most of the *ab initio* calculations traditionally used in AIRSS are replaced with MLP evaluations, significantly expanding the accessible search space thanks to the efficient computation of energies and forces provided by the MLP. To perform these global structure searches, we employ the RSSPOLYMLP code [71], which integrates RSS with polynomial MLPs.

2. Search space

Initial random structures for RSS are generated by randomly assigning lattice parameters and fractional atomic coordinates. Random structures are accepted only if they satisfy the main conditions of the Niggli-reduced cell [72] and meet a maximum volume constraint of 150 Å^3/atom. The degrees of freedom for structural optimization are restricted to cells containing up to 16 atoms. All possible combinations of atomic counts per element, $(n_\text{X}, n_\text{Bi})$, where n_X and n_Bi denote the number of atoms of element X and Bi per cell, respectively, are considered. In total, 152 combinations satisfying $1 \leq n_\text{X} + n_\text{Bi} \leq 16$ are included. RSS calculations for these compositions are performed at five pressure points up to 20 GPa, with a grid spacing of 5 GPa, resulting in 760 distinct conditions for each binary system. It should be noted that the current RSS procedure requires no prior structural knowledge, apart from specifying upper bounds on the cell volume and the number of atoms.

3. Computational Procedure

For one of the 760 conditions, RSS is conducted using the updated MLP, with local geometry optimizations repeated until 2,000 optimized structures are obtained. Across all conditions, this procedure yields approximately 1,520,000 local minimum structures. In addition, local geometry optimizations are performed starting from the local minimum structures obtained during the MLP update process to reduce the likelihood of missing any local minima. The total number of evaluations for energies, forces, and stress tensors reaches approximately three billion per binary system.

Using the set of distinct local minimum structures across all compositions at each pressure, the formation enthalpies and the corresponding convex hull are evaluated based on their MLP-predicted values. To improve the accuracy of the convex hull, DFT-based geometry optimizations are performed for a subset of local minimum structures. This subset includes structures with enthalpies relative to the MLP-derived convex hull, ΔH_ch, lower than a threshold value, θ. Additionally, DFT optimizations are carried out for experimentally reported structures that lie outside the current search space, in order to more reliably identify stable compounds in Bi-based systems. Experimental structures involving partial occupancies are excluded from consideration. All DFT geometry optimizations are performed under the computational settings described in Sec. II A 4.

To evaluate the pressure dependence of compound stability at finer pressure intervals, pressure–enthalpy relationships are calculated for compounds that are stable at one or more of the sampled pressure points. DFT calculations are performed to obtain energies at various volumes for these compounds. The resulting volume–energy data for each structure are fitted to the Rose–Vinet equation of state (EOS) [73] to derive the corresponding pressure–enthalpy relationships. Finally, convex hulls are constructed over a fine pressure grid with 0.01 GPa intervals, ranging from 0 to 20 GPa.

4. Computational notes

Table I summarizes the total number of local minimum structures with ΔH_ch values below a given threshold θ, obtained by summing the number of structures at pres-

TABLE I. Total number of local minimum structures with ΔH_{ch} values below various threshold values θ, calculated by summing the number of local minima identified at pressures of 0, 5, 10, 15, and 20 GPa. Bold values indicate the number of structures below the threshold values employed in this study. Geometry optimizations were performed using DFT for this screened set of structures, and their enthalpies were subsequently evaluated.

θ (meV/atom)	Na–Bi	K–Bi	Mg–Bi	Ca–Bi	Sr–Bi	Ba–Bi	Sc–Bi	Y–Bi	La–Bi	Eu–Bi	Gd–Bi
5	42	48	58	42	52	52	66	22	47	71	27
10	110	81	205	56	78	88	158	27	74	109	34
15	350	179	640	105	108	149	315	32	105	156	54
20	**1016**	454	**1754**	228	158	273	539	42	202	233	96
25	2330	**1230**	4082	489	281	566	796	87	380	388	202
30	4724	3051	8524	**941**	539	**1044**	**1262**	240	731	**687**	493
35	8148	5656	16264	1708	**919**	1675	2073	621	**1237**	1133	**1147**
40	13072	8475	28514	2728	1595	2561	3302	**1304**	1992	1870	2109
45	19217	11432	46663	3931	2467	3768	5168	2286	2854	2726	3381
50	26674	14790	70339	5612	3591	5392	8232	3594	3895	3790	5163

sures of 0, 5, 10, 15, and 20 GPa. The results indicate that a substantial number of structures exhibit formation enthalpies close to the convex hull. Therefore, the use of threshold values is necessary to limit the number of structures subjected to DFT calculations. We employ thresholds that are larger than the typical prediction errors for most structures in the dataset. The following thresholds are applied: 20 meV/atom for Na–Bi and Mg–Bi, 25 meV/atom for K–Bi, 30 meV/atom for Ca–Bi, Ba–Bi, Sc–Bi, and Eu–Bi, 35 meV/atom for Sr–Bi, La–Bi, and Gd–Bi, and 40 meV/atom for Y–Bi. For endmembers, the threshold is set to 20 meV/atom.

Although the search space is defined to include only local minimum structures containing up to 16 atoms, our structure search occasionally yields stable structures comprising more than 16 atoms. This arises from the standardization procedure applied during local geometry optimization. In this procedure, geometry optimization is first carried out on a randomly generated initial structure. The optimized structure is then transformed into a conventional unit cell based on its space group symmetry using a procedure implemented in the SPGLIB library [74]. A subsequent geometry optimization is performed on the standardized structure without using symmetry constraints. This cycle of optimization and standardization is repeated until both the enthalpy and atomic forces converge. During the standardization step, the transformation into a conventional cell can result in structures containing more than 16 atoms. Consequently, the search may converge to a local minimum structure that exceeds the initially defined atomic limit.

In MLP-based RSS, local minimum structures with unphysically low enthalpies and unusually short nearest-neighbor distances are occasionally predicted, even though the updated MLPs generally allow accurate enumeration of local minima. The presence of such structures prevents the identification of the true lowest-enthalpy configurations and complicates the reliable definition of screening thresholds. To address this issue, the following procedure is employed to eliminate unphysical structures. First, structures with unusually short nearest-neighbor distances are identified. Single-point DFT calculations are then performed for these structures. Structures exhibiting large errors in energies or stress tensors are subsequently discarded. The screening threshold is defined using the MLP enthapies of the remaining structures.

TABLE II. Accuracy and computational efficiency of the updated MLPs used for the global structure searches. The RMSEs are calculated using subsets of test datasets, excluding random structures generated with $\varepsilon > 0.2$ Å. The computational efficiency is assessed by measuring the elapsed time required to compute the energy, forces, and stress tensors of a structure containing 256 atoms. Since the computational cost scales linearly with the number of atoms, the elapsed time is normalized per atom. These calculations are performed using a single core of an Intel® Xeon® E5-2630 v3 (2.40 GHz), based on the implementation in the PYPOLYMLP code [48, 60].

	Energy RMSE (meV/atom)	Force RMSE (eV/Å)	Time (ms/atom/step)
Na–Bi	9.9	0.062	1.8
K–Bi	11.3	0.069	4.6
Mg–Bi	9.6	0.057	1.4
Ca–Bi	11.7	0.074	1.8
Sr–Bi	13.1	0.073	4.5
Ba–Bi	13.6	0.088	4.3
Sc–Bi	12.1	0.083	8.8
Y–Bi	10.3	0.087	8.2
La–Bi	10.7	0.085	8.2
Eu–Bi	11.9	0.086	4.8
Gd–Bi	10.8	0.094	4.5

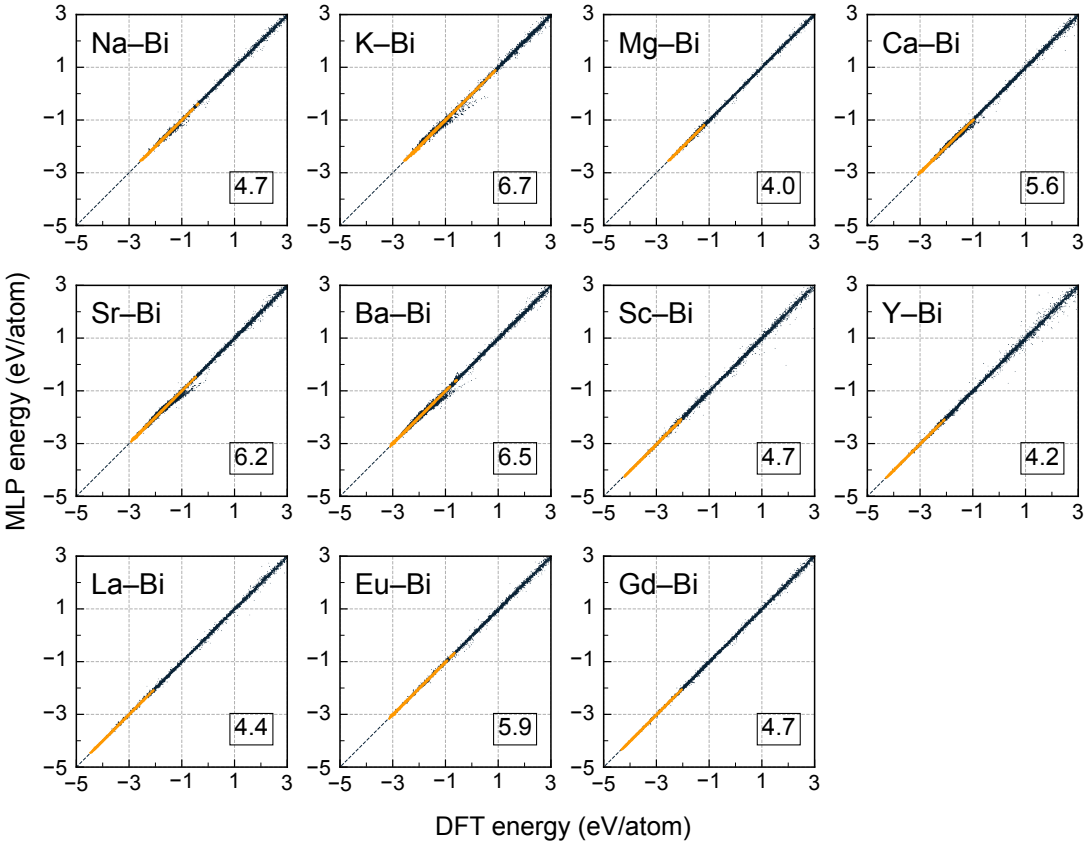

FIG. 1. Distributions of cohesive energy values for the DFT datasets in 11 Bi-based binary systems. These values are predicted using both DFT and the updated MLPs. The orange dots indicate the local minimum structures obtained through RSS during the second iteration of the MLP update process. The numerical values enclosed in squares represent the RMSEs of energy, expressed in meV/atom, estimated using the local minima shown as orange dots.

III. RESULTS AND DISCUSSION

A. MLP accuracy

Table II summarizes the prediction errors and computational efficiencies of the MLPs updated according to the procedure described in Sec. II A 3. The prediction errors are evaluated using the root mean square errors (RMSEs), calculated from a subset of the test dataset containing random structures generated with small deviations of $\varepsilon \leq 0.2$ Å. Here, ε is a parameter that controls the magnitudes of lattice expansion, distortion, and atomic displacements, as detailed in Appendix A. Since many of these random structures are close to local minima, their predictive performance is specifically assessed using the RMSE as defined above. The computational efficiency is assessed by measuring the elapsed time to compute the energy, forces, and stress tensors 20 times for a structure containing 256 atoms. The updated MLPs exhibit prediction accuracies of approximately 10 meV/atom for the energy RMSE and better than 0.1 eV/Å for the force RMSE across all systems for the random structures. Figure 1 compares the cohesive energy values for all structures in the dataset, calculated by both DFT and the updated MLP. The MLPs exhibit high predictive power across diverse structures, showing particularly low prediction errors for local minimum structures with enthalpy values close to the lowest at each composition, indicated by the orange dots in the figure.

B. Summary of global minimum structures

Tables III and IV summarize the predicted thermodynamically stable compounds identified through RSS using the MLP across 11 Bi-based binary systems, distinguishing between computationally predicted and experimentally reported compounds. Experimentally unreported compounds are indicated by filled circles. As shown in the tables, numerous compounds not previously reported in the literature have been discovered. These compounds are visualized later for the Na–Bi system, while the visualizations for the other systems are provided in the supplemental material. In the current structure search, all experimentally reported compounds that can be represented within a 16-atom cell are identified as either stable or metastable in the RSS results, highlighting the reliability of this approach. The stable structures

TABLE III. List of stable compounds predicted in this study across 11 Bi-based binary systems. Filled circles indicate predicted stable compounds that have not been reported experimentally in the literature, while open circles denote those that have been experimentally confirmed. In the formula column, X represents an element other than Bi, chosen from alkali metals, alkaline earth metals, rare-earth elements, or group 3 elements.

Formula	Prototype	Z	Space group	Alkali metals		Alkaline-earth metals				Rare-earth or group 3 elements				
				Na–Bi	K–Bi	Mg–Bi	Ca–Bi	Sr–Bi	Ba–Bi	Sc–Bi	Y–Bi	La–Bi	Eu–Bi	Gd–Bi
X_6Bi	—	14	$P\bar{1}$	—	—	—	—	—	—	●	—	—	—	—
X_5Bi	—	6	$P6/mmm$	—	●	—	—	—	—	—	—	—	—	—
	—	12	$P\bar{3}m1$	—	—	●	—	—	—	—	—	—	—	—
	—	12	$P\bar{1}$	—	—	—	—	—	—	●	—	—	—	—
X_4Bi	—	20	$C2/c$	—	—	—	—	—	—	●	—	—	—	—
$X_{11}Bi_3$	—	28	$Cmmm$	—	—	—	●	—	—	—	—	—	—	—
X_3Bi	$BiF_3(D0_3)$	16	$Fm\bar{3}m$	●	○	—	—	—	—	—	—	—	—	—
	$Na_3As(D0_{18})$	8	$P6_3/mmc$	○	—	—	—	—	—	—	—	—	—	—
	$LaF_3(D0_6)$	24	$P6_3cm$	—	○	—	—	—	—	—	—	—	—	—
	$Cu_3Au(L1_2)$	4	$Pm\bar{3}m$	—	—	●	●	●	●	—	—	●	●	●
	$Ni_3Sn(D0_{19})$	8	$P6_3/mmc$	—	—	—	—	○	—	—	—	—	●	—
	—	16	$P6_3/mmc$	—	—	—	—	●	—	—	—	—	—	—
	β–$TiCu_3(D0_a)$	8	$Pmmn$	—	—	—	—	—	—	●	—	—	—	—
	—	8	$P4/mbm$	—	—	—	—	—	—	—	—	—	●	—
X_5Bi_2	—	28	$C2/m$	—	—	●	—	—	—	—	—	—	—	—
X_7Bi_3	—	20	$I4/mmm$	—	—	●	—	—	—	—	—	—	—	—
	—	20	$C2/m$	—	—	●	—	—	—	—	—	—	—	—
X_9Bi_4	—	26	$C2/m$	—	—	—	—	—	●	—	—	—	—	—
X_2Bi	—	3	$P6/mmm$	—	●	—	—	—	—	—	—	—	—	—
	La_2Sb	12	$I4/mmm$	—	—	—	○	○	○	—	—	○	●	—
	—	12	$Cmmm$	—	—	—	●	●	—	—	—	—	●	—
	$InNi_2(B8_2)$	6	$P6_3/mmc$	—	—	—	—	—	●	—	—	—	—	—
	—	6	$I4/mmm$	—	—	—	—	—	●	—	—	—	—	—
	$Co_2Si(C37)$	12	$Pnma$	—	—	—	—	—	●	—	—	●	—	—
	$Cu_2Sb(C38)$	6	$P4/nmm$	—	—	—	—	—	—	●	—	—	—	—
	—	24	$C2/m$	—	—	—	—	—	—	—	—	●	●	—
	—	12	$Cmcm$	—	—	—	—	—	—	—	—	●	—	—
	—	24	$Cmce$	—	—	—	—	—	—	—	—	●	—	—
X_9Bi_5	—	28	$Cmmm$	—	—	—	—	—	—	—	—	●	—	—
X_5Bi_3	—	16	$P2_1/m$	—	—	●	—	—	—	—	—	—	—	—
	—	32	$Cmcm$	—	—	●	—	—	—	—	—	—	—	—
	—	32	$Pnma$	—	—	●	—	—	—	—	—	—	—	—
	$Mn_5Si_3(D8_8)$	16	$P6_3/mcm$	—	—	—	●	○	○	●	●	○	○	○
	—	16	$P\bar{1}$	—	—	—	●	●	—	—	—	—	●	—
	—	32	$I4/mcm$	—	—	—	—	—	●	—	—	—	—	—
	Yb_5Sb_3	32	$Pnma$	—	—	—	—	—	—	○	—	—	—	—
	—	16	$Immm$	—	—	—	—	—	—	—	—	●	—	—
X_3Bi_2	$La_2O_3(D5_2)$	5	$P\bar{3}m1$	—	—	○	—	—	—	—	—	—	—	—
	—	10	$P2_1/m$	—	—	●	—	—	—	—	—	—	—	—
	—	20	$Pnma$	—	—	●	—	—	—	—	—	—	—	—
	—	45	$R\bar{3}$	—	—	—	●	●	●	—	—	—	●	—
X_4Bi_3	$Th_3P_4(D7_3)$	28	$I\bar{4}3d$	—	—	—	●	○	○	●	●	○	○	○
	—	42	$R\bar{3}$	—	—	—	●	●	●	—	—	—	●	—
X_5Bi_4	—	18	$P2_1/c$	—	—	—	●	—	—	—	—	—	—	—
	—	36	$Cmce$	—	—	—	—	●	—	—	—	—	—	—
	—	36	$Pnma$	—	—	—	—	—	—	—	—	—	●	—
$X_{11}Bi_{10}$	$Ho_{11}Ge_{10}$	84	$I4/mmm$	—	—	—	○	○	○	—	—	—	○	—

TABLE IV. (cont.) List of stable compounds predicted in this study across 11 Bi-based binary systems.

Formula	Prototype	Z	Space group	Alkali metals		Alkaline-earth metals				Rare-earth or group-3 metals				
				Na–Bi	K–Bi	Mg–Bi	Ca–Bi	Sr–Bi	Ba–Bi	Sc–Bi	Y–Bi	La–Bi	Eu–Bi	Gd–Bi
XBi	CuAu(L1$_0$)	2	$P4/mmm$	○	●	—	●	●	—	—	—	○	●	—
	(CuAu(L1$_0$))	4	$P4/nmm$	—	—	—	—	—	—	—	—	●	—	—
	(CuAu(L1$_0$))	32	$Cmme$	—	—	—	—	—	—	—	—	●	—	—
	—	8	$Cmmm$	—	●	—	—	—	—	—	—	—	—	—
	—	16	$I4/mmm$	—	●	—	—	—	—	—	—	—	—	—
	KBi	32	$P2_1/c$	—	○	—	—	—	—	—	—	—	—	—
	—	14	$P2/m$	—	—	—	—	●	—	—	—	—	—	—
	—	14	$P2/m$	—	—	—	—	●	—	—	—	—	—	—
	CoAs	8	$Pmmn$	—	—	—	—	—	●	—	—	—	—	—
	—	8	$Pbam$	—	—	—	—	—	●	—	—	—	—	—
	—	8	$Pmma$	—	—	—	—	—	●	—	—	—	—	—
	NaCl(B1)	8	$Fm\bar{3}m$	—	—	—	—	—	—	○	○	○	—	○
	NiAs(B8$_1$)	4	$P6_3/mmc$	—	—	—	—	—	—	●	—	—	—	—
	FeSi(B20)	4	$P2_13$	—	—	—	—	—	—	●	—	—	—	—
	—	24	$R\bar{3}m$	—	—	—	—	—	—	●	—	—	—	—
	—	32	$Pnma$	—	—	—	—	—	—	—	●	—	—	●
	—	10	Pm	—	—	—	—	—	—	—	—	—	●	—
X_3Bi_4	—	14	$C2/m$	—	—	—	—	—	—	●	—	—	—	—
X_2Bi_3	Sr_2Bi_3	20	$Pnna$	—	—	—	—	○	—	—	—	—	—	—
	W_2CoB_2	10	$Immm$	—	—	—	—	—	○	—	—	—	—	—
	—	20	$C2/c$	—	—	—	—	—	●	—	—	—	—	—
X_3Bi_5	—	16	$Cmmm$	●	—	—	—	—	—	—	—	—	—	—
X_4Bi_7	—	22	$C2/m$	—	—	—	—	—	●	—	—	—	—	—
X_5Bi_9	—	28	$Cmmm$	—	—	—	—	—	●	—	—	—	—	—
XBi_2	$MgCu_2$(C15)	24	$Fd\bar{3}m$	—	○	—	—	—	—	—	—	—	—	—
	—	18	$C2/m$	—	—	●	—	—	—	—	—	—	—	—
	—	24	$I4/mcm$	—	—	●	—	—	—	—	—	—	—	—
	$ZrSi_2$(C49)	12	$Cmcm$	—	—	—	○	●	—	—	—	—	○	—
	—	6	$P2_1/m$	—	—	—	—	●	—	—	—	—	—	—
	—	12	$Cmcm$	—	—	—	—	—	●	—	—	—	—	—
	—	6	$I4/mmm$	—	—	—	—	—	—	●	—	—	—	—
	$PbCl_2$(C23)	12	$Pnma$	—	—	—	—	—	—	●	—	—	—	—
	$CrSi_2$(C40)	9	$P6_222$	—	—	—	—	—	—	—	●	—	—	●
	$CrSi_2$(C40)	9	$P6_422$	—	—	—	—	—	—	—	●	—	—	●
	—	24	$I4_1/amd$	—	—	—	—	—	—	—	—	●	—	—
	$HfGa_2$	24	$I4_1/amd$	—	—	—	—	—	—	—	—	—	○	—
X_3Bi_7	—	20	$Cmmm$	—	—	—	—	—	●	—	—	—	—	—
X_4Bi_{11}	—	30	$Immm$	—	—	—	—	—	—	●	—	—	—	—
XBi_3	Cu_3Au(L1$_2$)	4	$Pm\bar{3}m$	—	●	—	●	○	○	—	—	○	○	—
	—	4	$P6/mmm$	—	●	—	—	—	—	—	—	—	—	—
XBi_4	—	20	$Cmcm$	—	—	—	—	—	●	—	—	—	—	—
X_2Bi_9	—	22	$C2/m$	—	—	—	—	—	●	—	—	—	—	—
	—	33	$R\bar{3}m$	—	—	—	—	—	●	—	—	—	—	—
XBi_5	—	12	$Pmmn$	—	—	●	—	—	—	—	—	—	—	—
XBi_{12}	$Al_{12}W$	26	$Im\bar{3}$	●	—	—	—	—	—	—	—	—	—	—

TABLE V. Predicted stable compounds in the Na–Bi binary system. These compounds are predicted to be stable within the pressure ranges (in GPa) indicated in the "Pressure" column. Z denotes the number of atoms in the unit cell. The "ICSD-ID" column lists the corresponding identifiers in the ICSD. The "Prototype" column indicates known prototype structures adopted by the predicted compounds.

Formula	Space group	Z	ICSD-ID	Prototype	Pressure
Na_3Bi	$P6_3/mmc$	8	26881	$Na_3As(D0_{18})$	0.0–0.7
	$Fm\bar{3}m$	16	—	$BiF_3(D0_3)$	0.7–20.0
NaBi	$P4/mmm$	2	58816	$CuAu(L1_0)$	0.0–20.0
Na_3Bi_5	$Cmmm$	16	—	—	0.0–5.1
$NaBi_{12}$	$Im\bar{3}$	26	—	$Al_{12}W$	2.9–13.2

TABLE VI. Predicted stable compounds in the K–Bi binary system. The column definitions are the same as in Table V. Compounds reported in the ICSD but not obtained through RSS, since they are beyond the search space, are indicated by parentheses in the "Pressure" column. In addition, experimentally reported compounds predicted to be metastable are also listed; their corresponding pressure ranges are left blank.

Formula	Space group	Z	ICSD-ID	Prototype	Pressure
K_5Bi	$P6/mmm$	6	—	—	14.7–20.0
K_3Bi	$P6_3cm$	24	409223	$LaF_3(D0_6)$	(0.0–0.8)
	$Fm\bar{3}m$	16	58793	$BiF_3(D0_3)$	0.8–20.0
K_2Bi	$P6/mmm$	3	—	—	1.6–20.0
KBi	$P2_1/c$	32	55065	KBi	(0.0–0.6)
	$I4/mmm$	16	—	—	0.6–1.8
	$Cmmm$	8	—	—	1.8–2.2
	$P4/mmm$	2	—	$CuAu(L1_0)$	2.2–20.0
KBi_2	$Fd\bar{3}m$	24	55068	$MgCu_2(C15)$	0.0–5.4
KBi_3	$P6/mmm$	4	—	—	2.1–13.1
	$Pm\bar{3}m$	4	—	$Cu_3Au(L1_2)$	13.1–20.0
K_3Bi	$P6_3/mmc$	8	26885	$Na_3As(D0_{18})$	—

of the elemental endmembers are provided in the supplemental material.

Although a wide variety of structures are identified in the present search, 19 distinct compound types, defined by the structure type and the element ratio, are observed across different binary systems. Notably, the Mn_5Si_3-type X_5Bi_3 and Th_3P_4-type X_4Bi_3 are stable in eight different systems. Among these, the compounds in the Ca–Bi, Sc–Bi, and Y–Bi systems are newly discovered in this study. In addition, the Cu_3Au-type X_3Bi, CuAu-type XBi, and Cu_3Au-type XBi_3 are predicted to be stable in several systems. Furthermore, many compound types that have not yet been experimentally reported in Bi-based systems are computationally identified as stable across multiple systems. These include the Cu_3Au-type X_3Bi; the Co_2Si-type, $Cmmm$, and $C2/m$ structures for X_2Bi; the $P\bar{1}$ structure of X_5Bi_3; the $R\bar{3}$ structure of X_3Bi_2; the $R\bar{3}$ structure of X_4Bi_3; the $Pnma$ structure of XBi; and the $CrSi_2$-type XBi_2.

C. Na–Bi

In the Na–Bi system, two compounds have been experimentally reported and are listed in the ICSD [76, 77]: Na_3Bi, which adopts the Na_3As-type structure, and NaBi, which crystallizes in the CuAu-type structure. Na_3Bi at ambient pressure is known to be a topological Dirac semimetal [34], while CuAu-type NaBi exhibits superconductivity [36].

Figure 2(a) shows the formation enthalpies predicted by the MLP for local minimum structures identified through MLP-based RSS. This result demonstrates that RSS efficiently generates a large number of local minima across the entire compositional range. The figure also presents the MLP-calculated formation enthalpies for a selected subset of local minimum structures that lie close to the convex hull. Similarly, Fig. 2(b) shows the formation enthalpies calculated using DFT for the same subset, providing more reliable values than those obtained from the MLP in Fig. 2(a). These DFT formation enthalpies are obtained after full geometry optimizations. As shown in Figs. 2(a) and (b), the convex hulls predicted by the MLP closely match those obtained from DFT calculations, confirming that the combination of RSS and MLP provides an accurate and efficient approach for identifying thermodynamically relevant local minimum structures.

Table V lists the predicted thermodynamically stable compounds in the Na–Bi system, along with the corresponding pressure ranges over which they are stable. Figure 3 illustrates these stable compounds. Both experimentally reported compounds are found to be stable in the present search. Our calculations further predict the existence of crystalline polymorphs and indicate that Na_3Bi, which adopts the Na_3As-type structure at ambient pressure, exhibits a transition to the BiF_3-type structure at 0.7 GPa. Additionally, two previously unreported compounds are identified: Na_3Bi_5 with space group $Cmmm$ and $NaBi_{12}$ adopting the $Al_{12}W$-type structure.

D. K–Bi

In the K–Bi system, five compounds have been reported and are listed in the ICSD [76, 78–80]. The $MgCu_2$-type KBi_2 is known to exhibit superconductivity [37]. For K_3Bi, polymorphs have been reported: the LaF_3-type structure is stable below 553 K, while the BiF_3-type appears as a high-temperature phase. In addition, the Na_3As-type K_3Bi has been theoretically predicted to be a topological Dirac semimetal based on *ab initio* calculations [35].

Figure 4 presents the formation enthalpies calculated

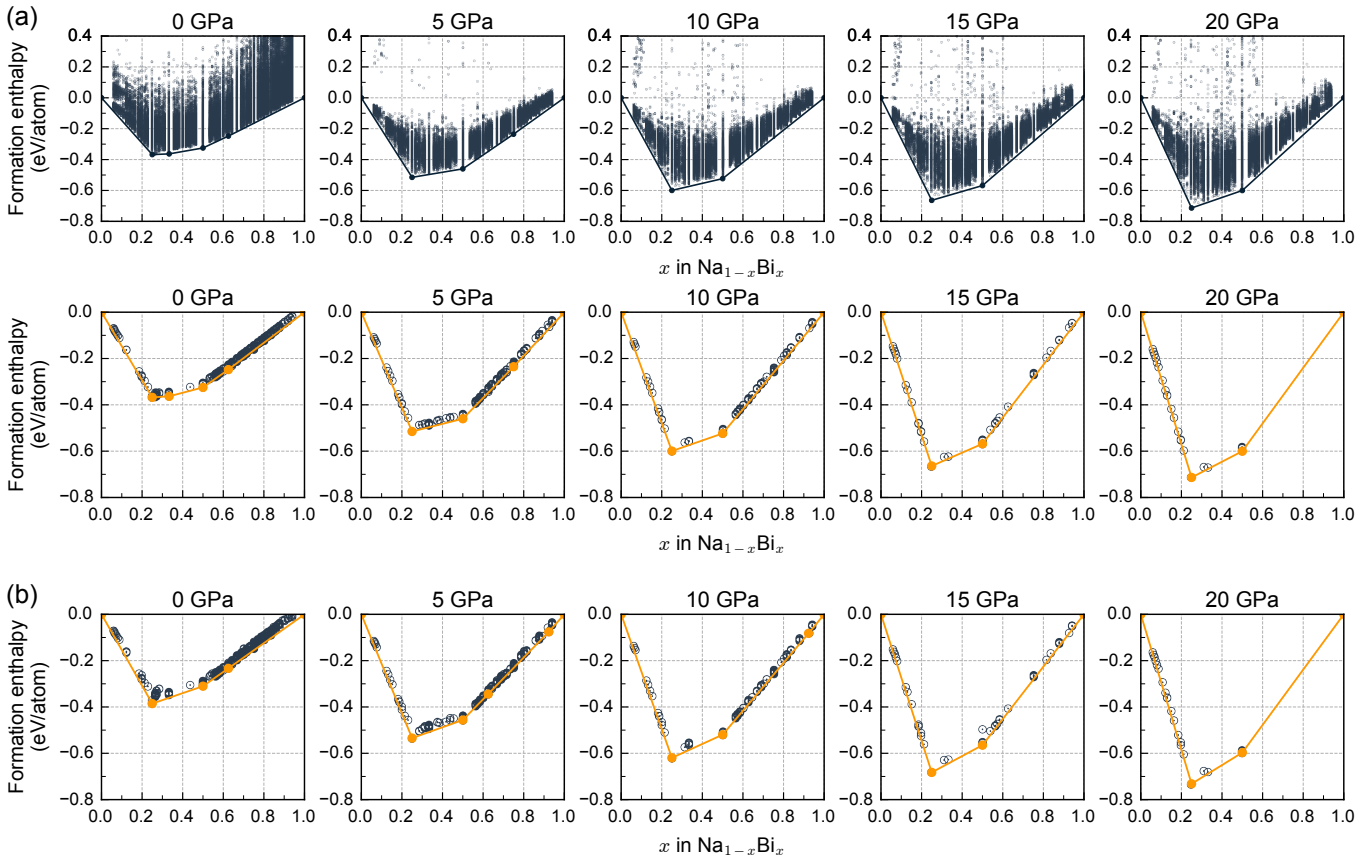

FIG. 2. (a) Formation enthalpies predicted using the MLP for local minimum structures generated with MLP-based RSS in the Na–Bi system, shown in the upper panel. The lower panel presents the formation enthalpies of a subset of local minima with ΔH_{ch} values below 20 meV/atom. (b) Formation enthalpies calculated using DFT for the subset of structures shown in the lower panel of (a). These structures were fully optimized using DFT.

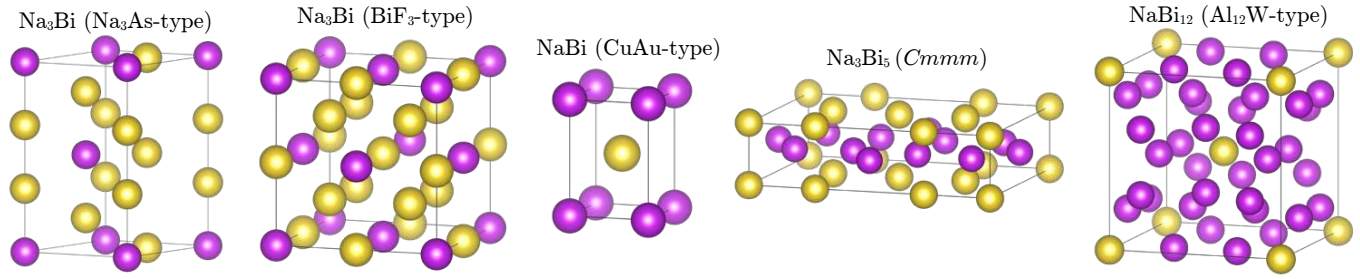

FIG. 3. Crystal structures of the globally stable compounds in the Na–Bi system. Yellow and purple spheres represent Na and Bi atoms, respectively. These structures are visualized using VESTA [75].

using DFT for a subset of local minimum structures near the convex hull, identified through MLP-based RSS. The formation enthalpies predicted by the MLP for a much larger set of local minima are provided in the supplemental material.

Table VI lists the thermodynamically stable compounds identified through the present structure search, and these stable compounds are visualized in the supplemental material. While the experimentally reported Na_3As-type K_3Bi is predicted to be metastable, the other known compounds are found to be stable. In addition, seven previously unreported stable compounds are discovered under pressure conditions at the compositions of K_5Bi, K_2Bi, KBi, and KBi_3. Polymorphs are also identified for KBi and KBi_3. For KBi, the experimentally reported KBi-type structure is stable in the pressure range of 0–0.6 GPa, followed by successive stabilization of structures with space groups $I4/mmm$, $Cmmm$, and $P4/mmm$ (CuAu-type) as pressure increases. In the case of KBi_3, the $P6/mmm$ structure is predicted to be stable

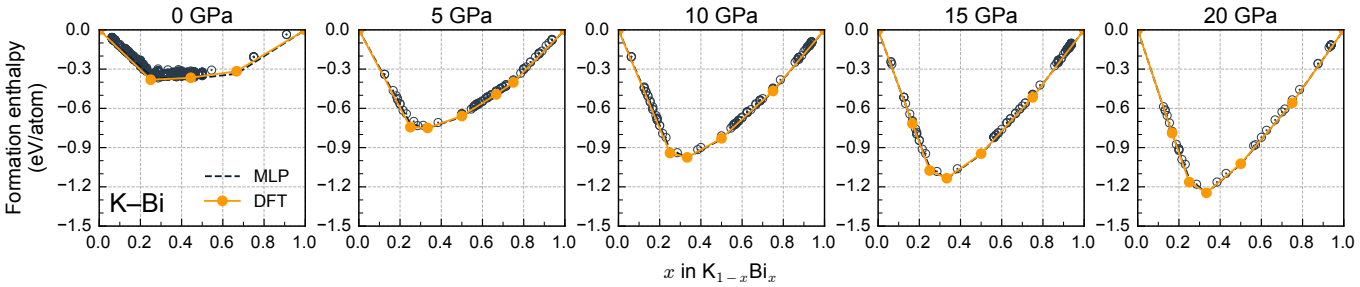

FIG. 4. Formation enthalpies of local minimum structures in the K–Bi system, calculated using DFT. The black dashed lines and solid orange lines represent the convex hulls constructed using the MLP and DFT, respectively.

TABLE VII. Predicted stable compounds in the Mg–Bi binary system. The column definitions are the same as in Table V.

Formula	Space group	Z	ICSD-ID	Prototype	Pressure
Mg_5Bi	$P\bar{3}m1$	12	—	—	11.4–14.7
Mg_3Bi	$Pm\bar{3}m$	4	—	$Cu_3Au(L1_2)$	13.7–20.0
Mg_5Bi_2	$C2/m$	28	—	—	11.1–20.0
Mg_7Bi_3	$I4/mmm$	20	—	—	1.3–3.1
	$C2/m$	20	—	—	3.1–20.0
Mg_5Bi_3	$Cmcm$	32	—	—	1.5–2.0
	$P2_1/m$	16	—	—	2.0–6.9
	$Pnma$	32	—	—	6.9–20.0
Mg_3Bi_2	$P\bar{3}m1$	5	659569	$La_2O_3(D5_2)$	0.0–2.0
	$P2_1/m$	10	—	—	2.0–7.0
	$Pnma$	20	—	—	7.0–20.0
$MgBi_2$	$I4/mcm$	24	—	—	6.6–9.4
	$C2/m$	18	—	—	9.4–20.0
$MgBi_5$	$Pmmn$	12	—	—	1.9–11.8

between 2.1 and 13.1 GPa, showing a transition to the Cu_3Au-type structure above 13.1 GPa.

E. Mg–Bi

In the Mg–Bi system, only one compound, Mg_3Bi_2 with the La_2O_3-type structure [81], has been experimentally reported in the ICSD. An experimental study further revealed that this compound exhibits a phase transition to a structure with space group $C2/m$ at approximately 4.0 GPa [82].

Figure 5 presents the formation enthalpies computed by DFT for a subset of local minimum structures obtained through RSS. Although the convex hull computed by the MLP at zero pressure shows slight deviations from the DFT-derived convex hull near the composition of Mg_3Bi_2, the convex hulls calculated using MLP at higher pressures agree with those verified by DFT. The supplemental material provides the MLP-predicted formation enthalpies for a wide range of local minima, demonstrating that RSS identifies a large number of candidate structures across all compositions.

Table VII summarizes the predicted thermodynamically stable compounds in the Mg–Bi system, which are visualized in the supplemental material. At zero pressure, only the experimentally reported La_2O_3-type Mg_3Bi_2 is predicted to be stable. Under pressure, however, additional stable compounds are identified at various compositions, including Mg_5Bi, Mg_3Bi, Mg_5Bi_2, Mg_7Bi_3, Mg_5Bi_3, Mg_3Bi_2, $MgBi_2$, and $MgBi_5$. Furthermore, the thermodynamically stable structures of Mg_7Bi_3, Mg_5Bi_3, Mg_3Bi_2, and $MgBi_2$ vary with pressure. In the case of Mg_3Bi_2, our calculations predict a sequence of pressure-induced transitions that differs from the experimentally reported transition to the $C2/m$ structure [82]. The stable structure is predicted to evolve from the La_2O_3-type structure to a $P2_1/m$ structure, and subsequently to a $Pnma$ structure. The experimentally reported $C2/m$ structure is identified as metastable in our search.

F. Ca–Bi

In the Ca–Bi system, four compounds have been experimentally reported in the ICSD [83–86]. Among these compounds, the $ZrSi_2$-type $CaBi_2$ has been reported to exhibit superconductivity [39]. Furthermore, superconductivity has also been observed in the defective $Ho_{11}Ge_{10}$-type $Ca_{11}Bi_{10-x}$ [38].

Figure 6 shows DFT-calculated formation enthalpies for a subset of local minimum structures obtained through RSS. The supplemental material provides the formation enthalpies predicted by the MLP for local minimum structures. Table VIII summarizes the predicted stable compounds and the corresponding pressure ranges over which these compounds are thermodynamically stable. Visualizations of these compounds are provided in the supplemental material. The experimentally reported Yb_5Sb_3-type Ca_5Bi_3 is found to be metastable in the present study, whereas the other experimentally reported compounds are identified as stable. In addition, numerous experimentally unreported compounds are predicted in this work.

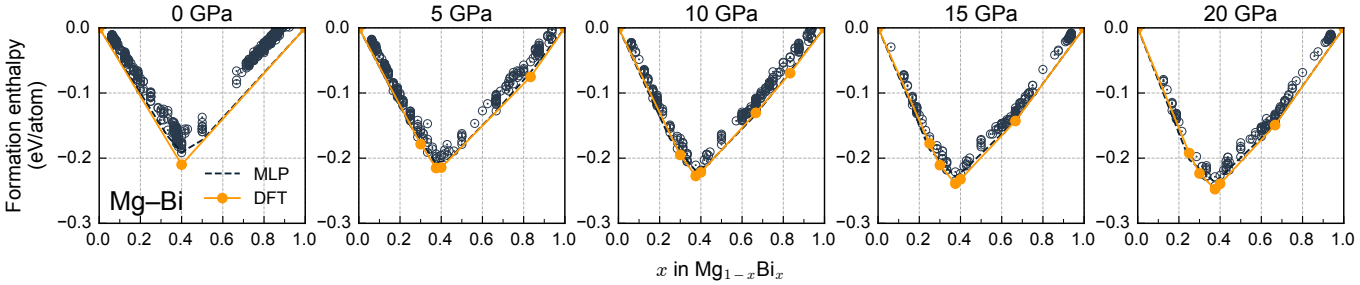

FIG. 5. Formation enthalpies of local minimum structures in the Mg–Bi system, calculated using DFT. The black dashed lines and solid orange lines represent the convex hulls constructed using the MLP and DFT, respectively.

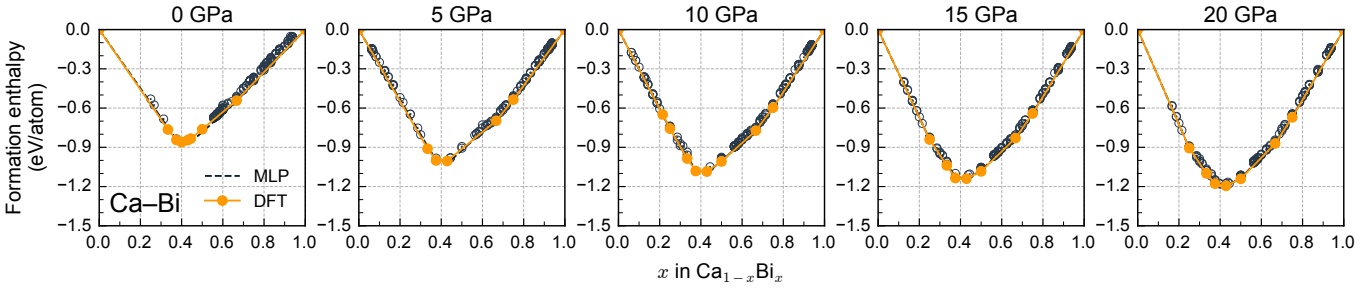

FIG. 6. Formation enthalpies of local minimum structures in the Ca–Bi system, calculated using DFT. The black dashed lines and solid orange lines represent the convex hulls constructed using the MLP and DFT, respectively.

TABLE VIII. Predicted stable compounds in the Ca–Bi binary system. The column definitions are the same as in Tables V and VI.

Formula	Space group	Z	ICSD-ID	Prototype	Pressure
$Ca_{11}Bi_3$	$Cmmm$	28	—	—	8.1–10.4
Ca_3Bi	$Pm\bar{3}m$	4	—	$Cu_3Au(L1_2)$	8.5–20.0
Ca_2Bi	$I4/mmm$	12	42136	La_2Sb	0.0–14.4
	$Cmmm$	12	—	—	14.4–20.0
Ca_5Bi_3	$P6_3/mcm$	16	—	$Mn_5Si_3(D8_8)$	0.0–18.3
	$P\bar{1}$	16	—	—	18.3–20.0
Ca_3Bi_2	$R\bar{3}$	45	—	—	0.0–1.2
Ca_4Bi_3	$I\bar{4}3d$	28	—	$Th_3P_4(D7_3)$	0.0–16.3
	$R\bar{3}$	42	—	—	16.3–20.0
Ca_5Bi_4	$P2_1/c$	18	—	—	10.2–18.3
$Ca_{11}Bi_{10}$	$I4/mmm$	84	434	$Ho_{11}Ge_{10}$	(0.0–11.3)
CaBi	$P4/mmm$	2	—	$CuAu(L1_0)$	9.7–20.0
$CaBi_2$	$Cmcm$	12	659277	$ZrSi_2(C49)$	0.0–20.0
$CaBi_3$	$Pm\bar{3}m$	4	—	$Cu_3Au(L1_2)$	1.8–20.0
Ca_5Bi_3	$Pnma$	32	2140	Yb_5Sb_3	—

A DFT-based global structure search under both ambient and high-pressure conditions for the Ca–Bi system has been previously reported in the literature [32]. At the Ca_3Bi_2 composition, the prior study found that the La_2O_3-type structure is stable at 0.0–4.0 GPa, and that it transforms into a $C2/m$ structure at pressures above 4.0 GPa. In contrast, the present results indicate that a thermodynamically stable compound exists only within the pressure range of 0.0–1.2 GPa at this composition, and its structure corresponds to the $R\bar{3}$ space group. Although the La_2O_3-type and $C2/m$ structures proposed in the previous study are also identified in the current structure search, they are evaluated as metastable, having higher enthalpy than the $R\bar{3}$ structure. This $R\bar{3}$ structure shares the same structure type as the stable structure of Sr_3Bi_2 previously predicted by a DFT-based global structure search [33]. It is also identified as stable in both the Sr–Bi and Ba–Bi systems in the present work, as discussed later. In addition to this compound, several thermodynamically stable compounds not reported in Ref. [32] are found in the present work. These include the $Cmmm$ $Ca_{11}Bi_3$, the Mn_5Si_3-type Ca_5Bi_3, the $P\bar{1}$ Ca_5Bi_3, the Th_3P_4-type Ca_4Bi_3, the $R\bar{3}$ Ca_4Bi_3, and the $P2_1/c$ Ca_5Bi_4. These findings underscore the significance of comprehensive structure enumeration based on MLPs for the robust and reliable identification of global minima.

G. Sr–Bi

In the Sr–Bi system, seven compounds have been experimentally reported in the ICSD [85, 87–90]. Among these, the Cu_3Au-type $SrBi_3$ is known to exhibit superconductivity [40]. In addition, Sr_3Bi_2 with the $R\bar{3}$ structure, which has not been experimentally reported, is theoretically predicted to be a three-dimensional topological insulator [33].

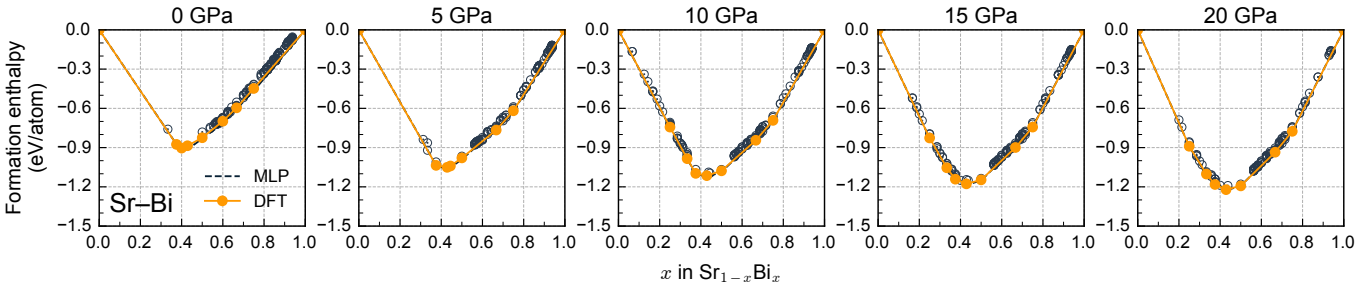

FIG. 7. Formation enthalpies of local minimum structures in the Sr–Bi system, calculated using DFT. The black dashed lines and solid orange lines represent the convex hulls constructed using the MLP and DFT, respectively.

TABLE IX. Predicted stable compounds in the Sr–Bi binary system. The column definitions are the same as in Tables V and VI.

Formula	Space group	Z	ICSD-ID	Prototype	Pressure
Sr_3Bi	$Pm\bar{3}m$	4	—	$Cu_3Au(L1_2)$	9.6–16.4
	$P6_3/mmc$	16	—	—	16.4–19.0
	$P6_3/mmc$	8	—	$Ni_3Sn(D0_{19})$	19.0–20.0
Sr_2Bi	$I4/mmm$	12	41836	La_2Sb	5.2–10.4
	$Cmmm$	12	—	—	10.4–20.0
Sr_5Bi_3	$P6_3/mcm$	16	617154	$Mn_5Si_3(D8_8)$	0.0–12.7
	$P\bar{1}$	16	—	—	12.7–20.0
Sr_3Bi_2	$R\bar{3}$	45	—	—	0.0–1.7
Sr_4Bi_3	$I\bar{4}3d$	28	96944	$Th_3P_4(D7_3)$	1.0–10.8
	$R\bar{3}$	42	—	—	10.8–20.0
Sr_5Bi_4	$Cmce$	36	—	—	0.0–3.1
$Sr_{11}Bi_{10}$	$I4/mmm$	84	659276	$Ho_{11}Ge_{10}$	(0.0–11.6)
SrBi	$P2/m$	14	—	—	8.2–11.6
	$P4/mmm$	2	—	$CuAu(L1_0)$	11.6–18.1
	$P2/m$	14	—	—	18.1–20.0
Sr_2Bi_3	$Pnna$	20	106329	Sr_2Bi_3	(0.0–2.4)
$SrBi_2$	$P2_1/m$	6	—	—	0.0–1.7
	$Cmcm$	12	—	$ZrSi_2(C49)$	1.7–20.0
$SrBi_3$	$Pm\bar{3}m$	4	58858	$Cu_3Au(L1_2)$	0.0–20.0
Sr_5Bi_3	$Pnma$	32	617155	Yb_5Sb_3	(—)

Figure 7 shows the DFT-calculated formation enthalpies for a subset of local minimum structures near the convex hull. The supplemental material provides the MLP-predicted formation enthalpies, revealing a large number of local minima across the full compositional range. Table IX summarizes the predicted thermodynamically stable compounds and the corresponding pressure ranges over which they are stable. These stable compounds are visualized in the supplemental material. The experimentally reported Yb_5Sb_3-type Sr_5Bi_3 is identified as metastable, while the other experimentally known compounds are found to be thermodynamically stable.

A DFT-based global structure search for the Sr–Bi system at zero pressure was also conducted in Ref. [33]. Both Sr_3Bi_2 and SrBi reported in the previous study are identified in the present work. The Sr_3Bi_2 compound with the $R\bar{3}$ space group, as calculated in Ref. [33], is predicted to be thermodynamically stable in the current study. In contrast, the SrBi reported in the previous study is identified as metastable. These differences arise from the significantly larger number of local minimum structures enumerated in the present study compared to the previous one, as shown in Fig. 7 and detailed in the supplemental material.

In addition to these previously reported theoretical compounds, the current study also predicts new stable compounds at zero pressure for other compositions, including the $Cmce$ Sr_5Bi_4 and the $P2_1/m$ $SrBi_2$. Furthermore, pressure-induced stabilization of previously unreported structures is predicted at the compositions Sr_3Bi, Sr_2Bi, Sr_5Bi_3, Sr_4Bi_3, SrBi, and $SrBi_2$. The thermodynamically stable structures at these compositions are also found to vary as a function of pressure. Notably, for Sr_2Bi, Sr_5Bi_3, and Sr_4Bi_3, the experimentally reported structures are predicted to undergo structural transformations under high-pressure conditions.

H. Ba–Bi

In the Ba–Bi system, six compounds have been experimentally reported in the ICSD [87, 88, 91–94]. Among these, the W_2CoB_2-type Ba_2Bi_3 and the $CuInPt_2$-type $BaBi_3$ have been reported to exhibit superconductivity [41, 42]. Additionally, Ba_3Bi_2 with the $R\bar{3}$ structure, which has not been experimentally reported, is theoretically predicted to be a three-dimensional topological insulator [33].

The formation enthalpies of local minimum structures calculated by DFT are shown in Fig. 8. The supplemental material provides MLP-predicted formation enthalpies for nearly all local minima, demonstrating that a large number of energetically distinct structures are obtained across a wide range of compositions.

Table X summarizes the predicted stable compounds and the corresponding pressure ranges over which these structures are thermodynamically stable. These stable compounds are visualized in the supplemental material. All experimentally reported compounds are identified as

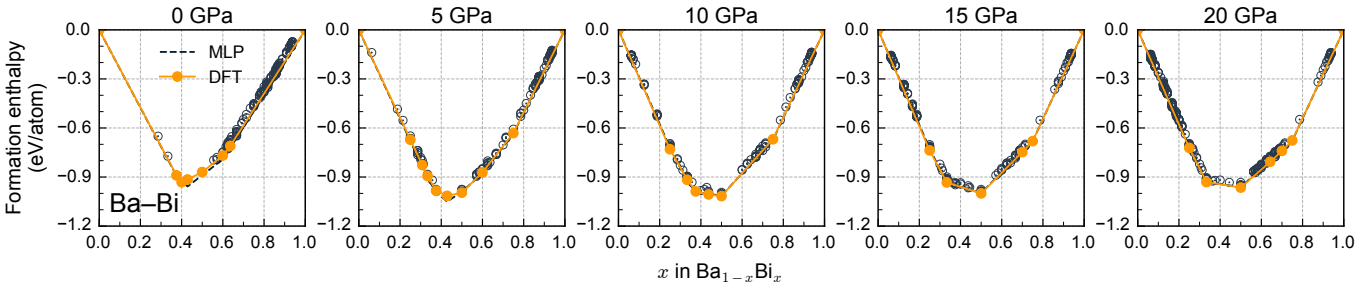

FIG. 8. Formation enthalpies of local minimum structures in the Ba–Bi system, calculated using DFT. The black dashed lines and solid orange lines represent the convex hulls constructed using the MLP and DFT, respectively.

TABLE X. Predicted stable compounds in the Ba–Bi binary system. The column definitions are the same as in Tables V and VI. Parentheses in the "ICSD-ID" and "Prototype" columns indicate that the corresponding compound is significantly similar to a known compound reported in the ICSD.

Formula	Space group	Z	ICSD-ID	Prototype	Pressure
Ba_3Bi	$Pm\bar{3}m$	4	—	$Cu_3Au(L1_2)$	5.0–20.0
Ba_9Bi_4	$C2/m$	26	—	—	4.0–5.2
Ba_2Bi	$I4/mmm$	12	2141	La_2Sb	2.1–4.3
	$Pnma$	12	—	$Co_2Si(C37)$	4.3–9.5
	$P6_3/mmc$	6	—	$InNi_2(B8_2)$	9.5–10.6
	$I4/mmm$	6	—	—	10.6–20.0
Ba_5Bi_3	$P6_3/mcm$	16	41839	$Mn_5Si_3(D8_8)$	0.0–4.4
	$I4/mcm$	32	—	—	4.4–14.3
Ba_3Bi_2	$R\bar{3}$	45	—	—	0.0–2.0
Ba_4Bi_3	$I\bar{4}3d$	28	96943	$Th_3P_4(D7_3)$	0.2–5.2
	$R\bar{3}$	42	—	—	5.2–15.6
$Ba_{11}Bi_{10}$	$I4/mmm$	84	51797	$Ho_{11}Ge_{10}$	(0–5.2)
BaBi	$Pmmn$	8	—	CoAs	0.0
	$Pbam$	8	—	—	3.6–7.4
	$Pmma$	8	—	—	7.4–20.0
Ba_2Bi_3	$Immm$	10	170218	W_2CoB_2	0.0–3.2
	$C2/c$	20	—	—	3.2–7.9
Ba_4Bi_7	$C2/m$	22	—	—	0.0–1.1
Ba_5Bi_9	$Cmmm$	28	—	—	16.8–20.0
$BaBi_2$	$Cmcm$	12	—	—	0.2–3.7
Ba_3Bi_7	$Cmmm$	20	—	—	9.9–20.0
$BaBi_3$	$Pm\bar{3}m$	4	(58634)	$(CuInPt_2)$	1.0–20.0
$BaBi_4$	$Cmcm$	20	—	—	0.8–1.2
Ba_2Bi_9	$C2/m$	22	—	—	0.7
	$R\bar{3}m$	33	—	—	0.7–0.8

stable in the present study. Although the $BaBi_3$ structure predicted here has a different space group from the experimentally reported structure with space group $P4/mmm$, their atomic configurations and enthalpies are nearly identical. In addition, numerous previously unreported compounds are predicted to be stable, and the stable structures of Ba_2Bi, Ba_5Bi_3, Ba_4Bi_3, $BaBi$, Ba_2Bi_3, and Ba_2Bi_9 are found to vary with increasing pressure. In particular, the experimentally reported Ba_2Bi, Ba_5Bi_3, Ba_4Bi_3, and Ba_2Bi_3 exhibit pressure-induced transitions to different structures under high-pressure conditions.

TABLE XI. Predicted stable compounds in the Sc–Bi binary system. The column definitions are the same as in Tables V and VI.

Formula	Space group	Z	ICSD-ID	Prototype	Pressure
Sc_6Bi	$P\bar{1}$	14	—	—	9.1–15.7
Sc_5Bi	$P\bar{1}$	12	—	—	13.7–16.4
Sc_4Bi	$C2/c$	20	—	—	12.3–20.0
Sc_3Bi	$Pmmn$	8	—	β–$TiCu_3(D0_a)$	16.5–20.0
Sc_2Bi	$P4/nmm$	6	—	$Cu_2Sb(C38)$	0.0–18.7
Sc_5Bi_3	$Pnma$	32	107590	Yb_5Sb_3	(0.0–9.9)
	$P6_3/mcm$	16	—	$Mn_5Si_3(D8_8)$	9.9–20.0
Sc_4Bi_3	$I\bar{4}3d$	28	—	$Th_3P_4(D7_3)$	5.7–20.0
ScBi	$P6_3/mmc$	4	—	$NiAs(B8_1)$	0.0–3.2
	$R\bar{3}m$	24	—	—	3.2–4.2
	$Fm\bar{3}m$	8	58856	NaCl(B1)	4.2–15.5
	$P2_13$	8	—	FeSi(B20)	15.5–20.0
Sc_3Bi_4	$C2/m$	14	—	—	14.7–17.5
$ScBi_2$	$Pnma$	12	—	$PbCl_2(C23)$	4.1–11.0
	$I4/mmm$	6	—	—	11.0–20.0
Sc_4Bi_{11}	$Immm$	30	—	—	2.9–20.0

I. Sc–Bi

Figure 9 presents the formation enthalpies computed by DFT for a subset of local minimum structures obtained via RSS. The supplemental material provides the formation enthalpies calculated using the MLP for nearly the entire set of local minima. Table XI summarizes the thermodynamically stable compounds predicted by the RSS procedure in the Sc–Bi system, and these compounds are visualized in the supplemental material.

In the Sc–Bi system, two structures have been experimentally reported in the ICSD: Sc_5Bi_3 with the Yb_5Sb_3-type structure [95] and ScBi with the NaCl-type struc-

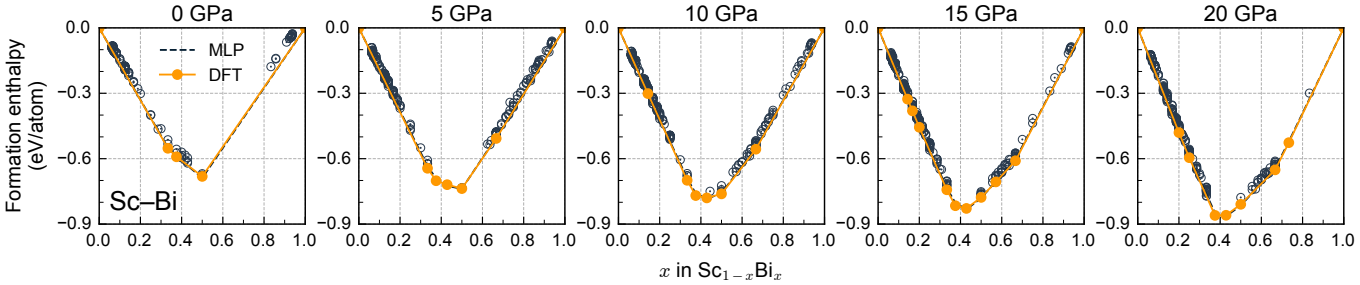

FIG. 9. Formation enthalpies of local minimum structures in the Sc–Bi system, calculated using DFT. The black dashed lines and solid orange lines represent the convex hulls constructed using the MLP and DFT, respectively.

TABLE XII. Predicted stable compounds in the Y–Bi binary system. The column definitions are the same as in Tables V and VI.

Formula	Space group	Z	ICSD-ID	Prototype	Pressure
Y_5Bi_3	$P6_3/mcm$	16	—	Mn_5Si_3($D8_8$)	0.0–20.0
Y_4Bi_3	$I\bar{4}3d$	28	—	Th_3P_4($D7_3$)	10.8–19.1
YBi	$Fm\bar{3}m$	8	58869	NaCl(B1)	0.0–14.7
	$Pnma$	32	—	—	14.7–20.0
YBi_2	$P6_222$	9	—	$CrSi_2$(C40)	1.3–20.0
	$P6_422$	9	—	$CrSi_2$(C40)	1.3–20.0
Y_5Bi_3	$Pnma$	32	77	Y_5Bi_3	(—)

ture [96]. Both of the experimentally reported compounds are reproduced as stable phases in our calculations. These phases are stable over the pressure ranges of 0.0–9.9 GPa and 4.2–15.5 GPa, respectively. In addition, several of the predicted stable compounds adopt known prototype structures. These include the β–$TiCu_3$-type Sc_3Bi, the Cu_2Sb-type Sc_2Bi, the Mn_5Si_3-type Sc_5Bi_3, the Th_3P_4-type Sc_4Bi_3, the NiAs- and FeSi-type ScBi, and the $PbCl_2$-type $ScBi_2$. For Sc_5Bi_3, ScBi, and $ScBi_2$, the thermodynamically stable structures are found to depend on pressure.

J. Y–Bi

In the Y–Bi system, two experimental compounds have been reported in the ICSD [97, 98], which are the NaCl-type YBi and Y_5Bi_3. In the NaCl-type YBi, extremely large magnetoresistance has been observed at low temperatures under high magnetic fields, and superconductivity has been reported under high-pressure conditions [44].

Figure 10 presents the formation enthalpies calculated by DFT for a subset of local minimum structures near the convex hull. The formation enthalpies for all local minima predicted by the MLP are provided in the supplemental material.

Table XII lists the stable compounds detected by the current structure search, along with the corresponding pressure ranges in which they are thermodynamically stable. These stable compounds are visualized in the supplemental material. The structure search predicts stable compounds at four distinct compositions in the Y–Bi system within the pressure range of 0–20 GPa. As found in Table XII, the experimentally reported NaCl-type YBi is predicted to be stable at 0–14.7 GPa, undergoing a transition to a structure with space group $Pnma$ above 14.7 GPa. In contrast, the experimental Y_5Bi_3 is found to be metastable in the current search, with the Mn_5Si_3-type structure being energetically more favorable. Additionally, some of the predicted compounds adopt known prototype structures, including the Th_3P_4-type Y_4Bi_3 and the $CrSi_2$-type YBi_2. The $CrSi_2$-type structure is chiral, and two enantiomorphic variants with space groups $P6_222$ and $P6_422$ are identified, exhibiting identical formation enthalpies.

K. La–Bi

In the La–Bi system, four structures have been experimentally reported in the ICSD [99]. Among them, the NaCl-type LaBi exhibits extremely large magnetoresistance under high magnetic fields and at low temperatures, and becomes superconducting above approximately 3.5 GPa [43]. This structure has also been experimentally reported to transform into the CuAu-type structure at around 11.0 GPa [43]. $LaBi_3$ has been reported to adopt the Cu_3Au-type structure at 3.4 GPa and to exhibit superconductivity [45].

Figure 11 shows the formation enthalpies calculated by DFT for a subset of local minimum structures near the convex hull obtained from RSS. The formation enthalpies predicted by the MLP for a broader set of local minima are provided in the supplemental material.

Table XIII summarizes the predicted thermodynamically stable compounds in the La–Bi system, which are visualized in the supplemental material. All the experimentally reported compounds are identified as stable in our calculations. In particular, the experimentally reported CuAu-type LaBi is predicted to be stable in the pressure range of 13.0–20.0 GPa, which is close to the experimentally observed phase transition pressure of ap-

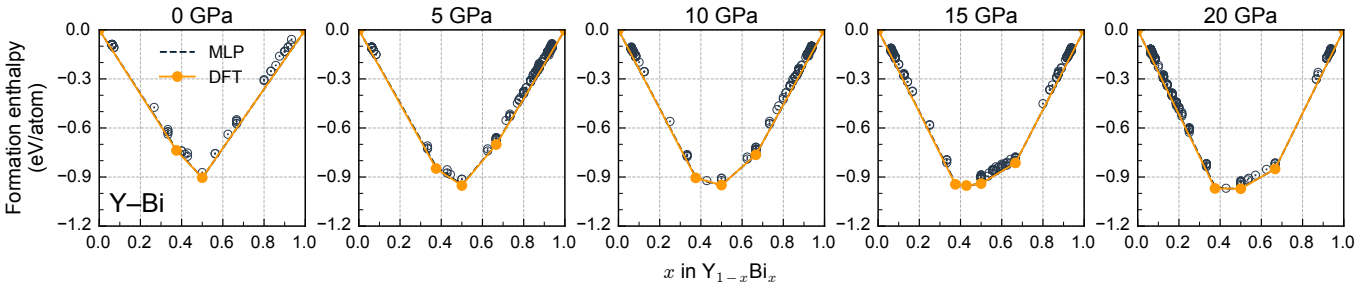

FIG. 10. Formation enthalpies of local minimum structures in the Y–Bi system, calculated using DFT. The black dashed lines and solid orange lines represent the convex hulls constructed using the MLP and DFT, respectively.

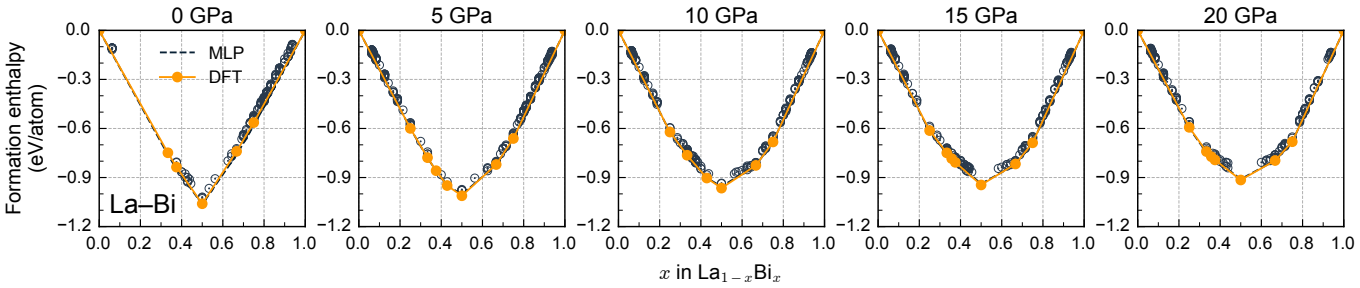

FIG. 11. Formation enthalpies of local minimum structures in the La–Bi system, calculated using DFT. The black dashed lines and solid orange lines represent the convex hulls constructed using the MLP and DFT, respectively.

TABLE XIII. Predicted stable compounds in the La–Bi binary system. The column definitions are the same as in Tables V and VI. Parentheses in the "Prototype" column indicate that each corresponding compound adopts a structure similar to a known prototype structure.

Formula	Space group	Z	ICSD-ID	Prototype	Pressure
La_3Bi	$Pm\bar{3}m$	4	—	$Cu_3Au(L1_2)$	3.7–20
La_2Bi	$I4/mmm$	12	616761	La_2Sb	0.0–0.8
	$Cmce$	24	—	—	0.8–7.9
	$C2/m$	24	—	—	7.9–12.5
	$Pnma$	12	—	$Co_2Si(C37)$	12.5–15.2
	$Cmcm$	12	—	—	15.2–20.0
La_9Bi_5	$Cmmm$	28	—	—	13.3–20.0
La_5Bi_3	$P6_3/mcm$	16	616760	$Mn_5Si_3(D8_8)$	0.0–8.0
	$Immm$	16	—	—	11.8–20.0
La_4Bi_3	$I\bar{4}3d$	28	616759	$Th_3P_4(D7_3)$	0.8–12.2
LaBi	$Fm\bar{3}m$	8	58795	NaCl(B1)	0.0–7.2
	$P4/nmm$	4	—	$(CuAu(L1_0))$	7.2–10.5
	$Cmme$	32	—	$(CuAu(L1_0))$	10.5–13.0
	$P4/mmm$	2	—	$CuAu(L1_0)$	13.0–20.0
$LaBi_2$	$I4_1/amd$	24	—	—	0.0–20.0
$LaBi_3$	$Pm\bar{3}m$	4	—	$Cu_3Au(L1_2)$	0.0–20.0

proximately 11.0 GPa. For LaBi, the structures with space groups $P4/nmm$ and $Cmme$ that are predicted to be stable at lower pressures are nearly identical to the CuAu-type structure. For other compositions, pressure-dependent stability is also observed. The experimentally reported La_2Sb-type La_2Bi is predicted to undergo a series of pressure-induced phase transitions above 0.8 GPa. With increasing pressure, structures with space groups $Cmce$, $C2/m$, $Pnma$ (Co_2Si-type), and $Cmcm$ are sequentially stabilized. In addition, for La_5Bi_3, where the experimentally reported Mn_5Si_3-type structure is stable at 0.0–8.0 GPa, a structure with space group $Immm$ becomes stable above 11.8 GPa.

L. Eu–Bi

In the Eu–Bi system, six compounds have been experimentally reported in the ICSD [85, 100–103]. The Cu_3Au-type $EuBi_3$ has also been reported in the literature as an experimentally synthesized compounds [104]. Figure 12 presents the formation enthalpies calculated by DFT for a subset of local minimum structures obtained through RSS. The supplemental material provides the formation enthalpies of local minimum structures predicted by the MLP.

Table XIV summarizes the predicted stable compounds in the Eu–Bi system and the corresponding pressure ranges over which these structures are thermodynamically stable. These compounds are visualized in the supplemental material. The experimentally reported Yb_5Sb_3-type Eu_5Bi_3 is predicted to be metastable, whereas the other experimentally reported compounds are identified as stable in our calculations. In addition, many of the predicted compounds adopt known

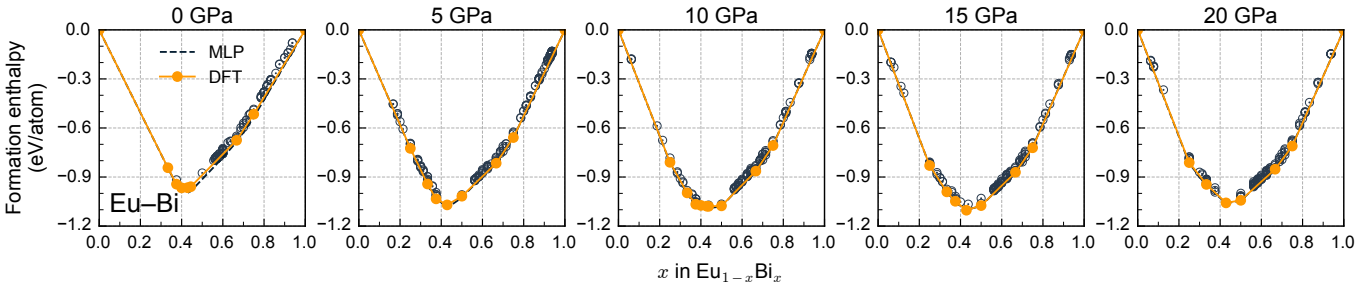

FIG. 12. Formation enthalpies of local minimum structures in the Eu–Bi system, calculated using DFT. The black dashed lines and solid orange lines represent the convex hulls constructed using the MLP and DFT, respectively.

TABLE XIV. Predicted stable compounds in the Eu–Bi binary system. The column definitions are the same as in Tables V and VI.

Formula	Space group	Z	ICSD-ID	Prototype	Pressure
Eu_3Bi	$Pm\bar{3}m$	4	—	$Cu_3Au(L1_2)$	4.0–9.3
	$P6_3/mmc$	8	—	$Ni_3Sn(D0_{19})$	9.3–12.0
	$P4/mbm$	8	—	—	12.0–20.0
Eu_2Bi	$I4/mmm$	12	—	La_2Sb	0.0–5.7
	$Cmmm$	12	—	—	5.7–11.9
	$C2/m$	24	—	—	11.9–20.0
Eu_5Bi_3	$P6_3/mcm$	16	173031	$Mn_5Si_3(D8_8)$	0.0–6.4
	$P\bar{1}$	16	—	—	6.4–18.7
Eu_3Bi_2	$R\bar{3}$	45	—	—	0.0–0.9
Eu_4Bi_3	$I\bar{4}3d$	28	199150	$Th_3P_4(D7_3)$	0.0–7.0
	$R\bar{3}$	42	—	—	7.0–20.0
Eu_5Bi_4	$Pnma$	36	—	—	0.0–1.6
$Eu_{11}Bi_{10}$	$I4/mmm$	84	616647	$Ho_{11}Ge_{10}$	(0.0–5.9)
EuBi	Pm	10	—	—	4.3–13.1
	$P4/mmm$	2	—	$CuAu(L1_0)$	13.1–20.0
$EuBi_2$	$Cmcm$	12	659278	$ZrSi_2(C49)$	0.0–16.0
	$I4_1/amd$	24	150347	$HfGa_2$	16.0–20.0
$EuBi_3$	$Pm\bar{3}m$	4	—	$Cu_3Au(L1_2)$	0.0–20.0
Eu_5Bi_3	$Pnma$	32	616646	Yb_5Sb_3	(—)

prototype structures. These include the Cu_3Au- and Ni_3Sn-type Eu_3Bi, the La_2Sb-type Eu_2Bi, and the CuAu-type EuBi. For several compositions, including Eu_3Bi, Eu_2Bi, Eu_5Bi_3, Eu_4Bi_3, EuBi, and $EuBi_2$, the thermodynamically stable structures are found to be pressure-dependent. In particular, the experimentally reported Eu_5Bi_3 and Eu_4Bi_3 are predicted to undergo pressure-induced structural transitions.

M. Gd–Bi

In the Gd–Bi system, five compounds have been experimentally reported in the ICSD [99, 105–107]. Among them, the NaCl-type GdBi exhibits extremely large magnetoresistance under low temperatures and high magnetic fields [46].

TABLE XV. Predicted stable compounds in the Gd–Bi binary system. The column definitions are the same as in Tables V and VI.

Formula	Space group	Z	ICSD-ID	Prototype	Pressure
Gd_3Bi	$Pm\bar{3}m$	4	—	$Cu_3Au(L1_2)$	15.0–20.0
Gd_5Bi_3	$P6_3/mcm$	16	58784	$Mn_5Si_3(D8_8)$	0.0–20.0
Gd_4Bi_3	$I\bar{4}3d$	28	616659	$Th_3P_4(D7_3)$	8.9–16.9
GdBi	$Fm\bar{3}m$	8	58783	NaCl(B1)	0.0–12.6
	$Pnma$	32	—	—	12.6–20.0
$GdBi_2$	$P6_222$	9	—	$CrSi_2(C40)$	0.6–20.0
	$P6_422$	9	—	$CrSi_2(C40)$	0.6–20.0
Gd_5Bi_3	$Pnma$	32	107262	Y_5Bi_3	(—)
	$Pnma$	32	616667	Yb_5Sb_3	(—)

Figure 13 presents the DFT formation enthalpies of a subset of local minimum structures near the convex hull obtained from RSS. The supplemental material presents the MLP-calculated formation enthalpies of local minima, revealing that an enormous number of local minimum structures are found across the composition range.

Table XV summarizes the predicted thermodynamically stable compounds identified by the present structure search, and these stable compounds are visualized in the supplemental material. The experimentally reported NaCl-type GdBi, the Mn_5Si_3-type Gd_5Bi_3, and the Th_3P_4-type Gd_4Bi_3 are predicted to be stable. In contrast, the Y_5Bi_3- and Yb_5Sb_3-type Gd_5Bi_3 are found to be metastable. Additionally, several predicted stable compounds adopt known prototype structures. For example, the Cu_3Au-type Gd_3Bi and the $CrSi_2$-type $GdBi_2$ are identified as stable, with the latter structure type also observed in the Y–Bi system. For GdBi, the thermodynamically stable structures are pressure-dependent. The NaCl-type structure of GdBi is predicted to transform into a structure with space group $Pnma$ above 12.6 GPa, consistent with the behavior observed in the Y–Bi system.

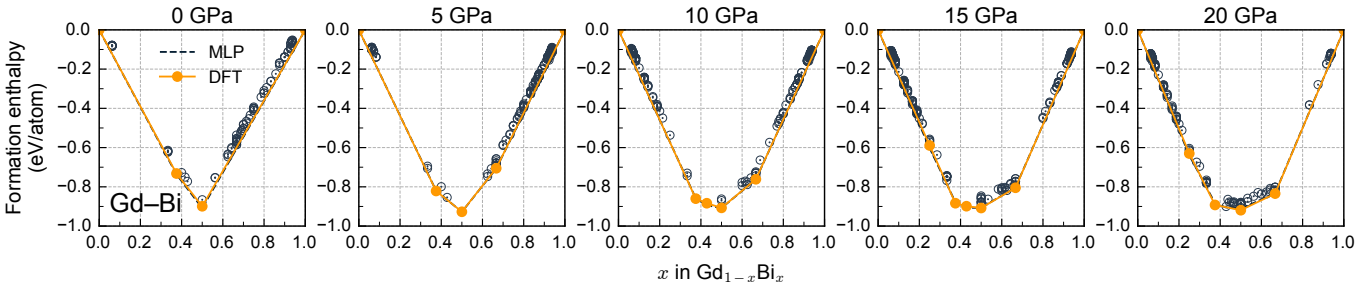

FIG. 13. Formation enthalpies of local minimum structures in the Gd–Bi system, calculated using DFT. The black dashed lines and solid orange lines represent the convex hulls constructed using the MLP and DFT, respectively.

IV. CONCLUSION

This study presents systematic predictions of stable and metastable compounds over the pressure range from 0 to 20 GPa for 11 Bi-based binary systems. To enable robust and efficient global structure exploration, accurate polynomial MLPs were developed for each system. Global structure searches performed using these MLPs enabled comprehensive sampling of the configurational space, involving billions of energy, force, and stress tensor evaluations. As a result, all experimentally known structures within the considered search space were reproduced, highlighting the reliability and predictive power of the current approach. Moreover, numerous previously unreported compounds were identified. The predicted compounds provide valuable insights for guiding the discovery and design of new materials in these systems under both ambient and high-pressure conditions.

ACKNOWLEDGMENTS

This work was supported by a Grant-in-Aid for Japan Society for the Promotion of Science (JSPS) Fellows (Grant Number 25KJ1602), a Grant-in-Aid for Scientific Research (S) (Grant Number 25H00420), and a Grant-in-Aid for Challenging Research (Exploratory) (Grant Number 25K22169) from the JSPS. This work was also supported by the Iketani Science and Technology Foundation.

Appendix A: Generation of initial dataset

Here, we describe the procedure for constructing the initial dataset used to develop a polynomial MLP capable of robust and efficient global structure searches. In this approach, random structures are generated from equilibrium prototype structures optimized by DFT calculations. Let $\boldsymbol{A}$ denote the matrix of lattice vectors for a prototype structure, and let $\boldsymbol{f}$ represent the vector of fractional coordinates of an atom within the structure. The lattice vector matrix $\boldsymbol{A'}$ and the fractional coordinates $\boldsymbol{f'}$ of the atom in a randomly generated structure are defined as follows:

$$\begin{aligned} \boldsymbol{A'} &= \boldsymbol{A} + \varepsilon \boldsymbol{R}, \\ \boldsymbol{f'} &= \boldsymbol{f} + \varepsilon \boldsymbol{A'}^{-1} \boldsymbol{\eta}, \end{aligned} \tag{A1}$$

where $\boldsymbol{R}$ is a three-dimensional square matrix and $\boldsymbol{\eta}$ is a three-dimensional vector, both composed of uniformly distributed random numbers in the range $[-1, 1]$. The parameter ε controls the magnitudes of lattice expansion, distortion, and atomic displacements. When generating N_{st} random structures from a given prototype, the value of ε for the Nth structure, denoted as ε_N, is defined by a finite arithmetic progression as $\varepsilon_N = \varepsilon_{\max} N / N_{\mathrm{st}}$.

The parameter settings used for random structure generation are as follows. First, DFT geometry optimizations are performed for the prototype structures under two pressure conditions: 0 GPa and 20 GPa. Subsequently, isotropic volume changes are applied to achieve specific volume ratios relative to the equilibrium volumes of the optimized prototype structures, prior to the generation of random configurations. For each prototype structure optimized at 0 GPa, random structures are generated at various volume ratios. Specifically, 10 random structures are generated at 80% and 90% of the equilibrium volume, 20 structures at the equilibrium volume, and 4 structures each at expanded volumes corresponding to 150%, 200%, and 300% of the equilibrium volume. For all these cases, the parameter $\varepsilon_{\max}$ is set to 1.0 Å.

For each prototype structure optimized at 20 GPa, a slightly different sampling strategy is employed. Isotropic volume changes are applied at volume ratios of 80%, 90%, and 100%, and random structures are generated using the same settings as those employed at 0 GPa for these volume conditions. In addition, an extreme compression case with a volume ratio of 20% is considered, for which a single random structure is generated using a reduced displacement parameter of $\varepsilon_{\max} = 0.1$ Å.

This dataset construction strategy facilitates the development of MLPs with predictive power not only for local minimum structures, but also for high-energy configurations exhibiting large atomic forces, which frequently arise during local geometry optimizations in RSS. Accurate prediction for such structures is essential for ensuring the stability and effectiveness of RSS-based global structure searches.

Appendix B: MLP estimation

The details of the MLP estimation procedure are provided in this section. The regression coefficients of a potential energy model are estimated through linear regression using the energy, force, and stress tensor values from the training dataset as observations. These quantities constitute the observation vector $\boldsymbol{y}$. The structural features used to represent the energy observations, such as polynomial invariants and their products, are included in the predictor matrix $\boldsymbol{X}$. Additionally, the derivatives of these features with respect to atomic positions and lattice vectors, which are required for calculating forces and stress tensors, are also incorporated into the predictor matrix $\boldsymbol{X}$:

$$\boldsymbol{X} = \begin{bmatrix} \boldsymbol{X}_{\text{energy}} \\ \boldsymbol{X}_{\text{force}} \\ \boldsymbol{X}_{\text{stress}} \end{bmatrix}, \quad \boldsymbol{y} = \begin{bmatrix} \boldsymbol{y}_{\text{energy}} \\ \boldsymbol{y}_{\text{force}} \\ \boldsymbol{y}_{\text{stress}} \end{bmatrix}. \tag{B1}$$

Here, $\boldsymbol{X}_{\text{energy}}$ represents the structural features, while $\boldsymbol{X}_{\text{force}}$ and $\boldsymbol{X}_{\text{stress}}$ consist of their derivatives with respect to atomic positions and lattice vectors, respectively. The observation vector $\boldsymbol{y}$ includes $\boldsymbol{y}_{\text{energy}}$, $\boldsymbol{y}_{\text{force}}$, and $\boldsymbol{y}_{\text{stress}}$, which contain total energies, forces, and stress tensor components from the DFT training dataset, respectively. Energy and stress tensor components are expressed in eV/cell, whereas force components are expressed in eV/Å.

The regression coefficients $\boldsymbol{w}$ are estimated using weighted linear ridge regression, formulated as

$$L(\boldsymbol{w}) = ||\boldsymbol{W}(\boldsymbol{X}\boldsymbol{w} - \boldsymbol{y})||_2^2 + \lambda||\boldsymbol{w}||_2^2. \tag{B2}$$

The solution for $\boldsymbol{w}$ is obtained by solving the normal equations

$$(\boldsymbol{X}^T\boldsymbol{W}^2\boldsymbol{X} + \lambda\boldsymbol{I})\boldsymbol{w} = \boldsymbol{X}^T\boldsymbol{W}^2\boldsymbol{y}. \tag{B3}$$

Here, $\boldsymbol{W}$ is a diagonal matrix whose entries assign weights to the energy, force, and stress tensor data. The regularization parameter λ is optimized to minimize prediction errors on the test dataset.

The weighting parameters applied to the energy, force, and stress tensor components are described below. A hierarchical procedure is employed to assign the weight values. Specifically, the weight assigned to the energy component of the i-th structure, $W(e_{[i]})$, is defined as

$$W(e_{[i]}) = \begin{cases} \zeta_{[i]} & (e_{[i]} < \theta_e) \\ 0.1\zeta_{[i]} & (e_{[i]} \geq \theta_e) \end{cases}, \tag{B4}$$

where $e_{[i]}$ denotes the total energy of the structure i, referenced to the energies of the isolated constituent atoms. The threshold value θ_e is set to 0 eV/cell. The weight for the force entry on α-component of the atom j in i-th structure, $W(f_{[i],j\alpha})$, is given as

$$W(f_{[i],j\alpha}) = \begin{cases} \zeta_{[i]} & (|f_{[i],j\alpha}| < \theta_f) \\ \dfrac{\zeta_{[i]}}{|f_{[i],j\alpha}|} & (|f_{[i],j\alpha}| \geq \theta_f) \end{cases}. \tag{B5}$$

Here, we set the threshold $\theta_f = 1$ eV/Å. The weight for the stress tensor entry, $W(\sigma_{[i],\beta\gamma})$, where $\sigma_{[i],\beta\gamma}$ denotes the stress component acting in the γ direction on a plane normal to the β direction in the i-th structure, is set as follows:

$$W(\sigma_{[i],\beta\gamma}) = 0.1\zeta_{[i]}. \tag{B6}$$

Relatively smaller weights are assigned to the stress tensor components compared to the energy entries, due to the inclusion of six independent stress components in the training process.

The scaling parameter $\zeta_{[i]}$ controls the structure-dependent magnitude of the weights and is determined based on the total energy $e_{[i]}$ as follows:

$$\zeta_{[i]} = \begin{cases} 1 & (e_{[i]} < \theta_e) \\ 0.1 & (\theta_e \leq e_{[i]} < \theta_e') \\ 0.01 & (e_{[i]} \geq \theta_e') \end{cases}. \tag{B7}$$

The threshold θ_e' is set to 10 eV/cell. With these settings, larger weights are assigned to data entries corresponding to lower energies and smaller forces, which is essential for accurately modeling the potential energy surface near local minima, while still ensuring acceptable accuracy for high-energy structures with large forces.

[1] S. Lorenz, A. Groß, and M. Scheffler, Representing high-dimensional potential-energy surfaces for reactions at surfaces by neural networks, Chem. Phys. Lett. **395**, 210 (2004).

[2] J. Behler and M. Parrinello, Generalized neural-network representation of high-dimensional potential-energy surfaces, Phys. Rev. Lett. **98**, 146401 (2007).

[3] J. Behler, Atom-centered symmetry functions for constructing high-dimensional neural network potentials, J. Chem. Phys. **134**, 074106 (2011).

[4] S. A. Ghasemi, A. Hofstetter, S. Saha, and S. Goedecker, Interatomic potentials for ionic systems with density functional accuracy based on charge densities obtained by a neural network, Phys. Rev. B **92**, 045131 (2015).

[5] N. Artrith and A. Urban, An implementation of artificial neural-network potentials for atomistic materials simulations: Performance for TiO2, Comput. Mater. Sci. **114**, 135 (2016).

[6] N. Artrith, A. Urban, and G. Ceder, Efficient and accurate machine-learning interpolation of atomic energies in compositions with many species, Phys. Rev. B **96**,

014112 (2017).
[7] B. Onat, E. D. Cubuk, B. D. Malone, and E. Kaxiras, Implanted neural network potentials: Application to Li-Si alloys, Phys. Rev. B **97**, 094106 (2018).
[8] J. Han, L. Zhang, R. Car, and E. Weinan, Deep potential: A general representation of a many-body potential energy surface, Commun. Comput. Phys. **23**, 629 (2018).
[9] R. Li, E. Lee, and T. Luo, A unified deep neural network potential capable of predicting thermal conductivity of silicon in different phases, Mater. Today Phys. **12**, 100181 (2020).
[10] A. P. Bartók, M. C. Payne, R. Kondor, and G. Csányi, Gaussian approximation potentials: The accuracy of quantum mechanics, without the electrons, Phys. Rev. Lett. **104**, 136403 (2010).
[11] W. J. Szlachta, A. P. Bartók, and G. Csányi, Accuracy and transferability of Gaussian approximation potential models for tungsten, Phys. Rev. B **90**, 104108 (2014).
[12] Z. Li, J. R. Kermode, and A. De Vita, Molecular Dynamics with On-the-Fly Machine Learning of Quantum-Mechanical Forces, Phys. Rev. Lett. **114**, 096405 (2015).
[13] A. Glielmo, P. Sollich, and A. De Vita, Accurate interatomic force fields via machine learning with covariant kernels, Phys. Rev. B **95**, 214302 (2017).
[14] A. P. Bartók, J. Kermode, N. Bernstein, and G. Csányi, Machine Learning a General-Purpose Interatomic Potential for Silicon, Phys. Rev. X **8**, 041048 (2018).
[15] A. Seko, A. Takahashi, and I. Tanaka, Sparse representation for a potential energy surface, Phys. Rev. B **90**, 024101 (2014).
[16] A. P. Thompson, L. P. Swiler, C. R. Trott, S. M. Foiles, and G. J. Tucker, Spectral neighbor analysis method for automated generation of quantum-accurate interatomic potentials, J. Comput. Phys. **285**, 316 (2015).
[17] A. V. Shapeev, Moment Tensor Potentials: A Class of Systematically Improvable Interatomic Potentials, Multiscale Model. Simul. **14**, 1153 (2016).
[18] C. Chen, Z. Deng, R. Tran, H. Tang, I.-H. Chu, and S. P. Ong, Accurate force field for molybdenum by machine learning large materials data, Phys. Rev. Mater. **1**, 043603 (2017).
[19] M. A. Wood and A. P. Thompson, Extending the accuracy of the SNAP interatomic potential form, J. Chem. Phys. **148**, 241721 (2018).
[20] A. Seko, A. Togo, and I. Tanaka, Group-theoretical high-order rotational invariants for structural representations: Application to linearized machine learning interatomic potential, Phys. Rev. B **99**, 214108 (2019).
[21] R. Drautz, Atomic cluster expansion for accurate and transferable interatomic potentials, Phys. Rev. B **99**, 014104 (2019).
[22] A. R. Oganov, J. Chen, C. Gatti, Y. Ma, Y. Ma, C. W. Glass, Z. Liu, T. Yu, O. O. Kurakevych, and V. L. Solozhenko, Ionic high-pressure form of elemental boron, Nature **457**, 863 (2009).
[23] C. J. Pickard and R. J. Needs, Ab initio random structure searching, J. Phys.: Condens. Matter **23**, 053201 (2011).
[24] J. Lv, Y. Wang, L. Zhu, and Y. Ma, Predicted novel high-pressure phases of lithium, Phys. Rev. Lett. **106**, 015503 (2011).
[25] W. Zhang, A. R. Oganov, A. F. Goncharov, Q. Zhu, S. E. Boulfelfel, A. O. Lyakhov, E. Stavrou, M. Somayazulu, V. B. Prakapenka, and Z. Konôpková, Unexpected stable stoichiometries of sodium chlorides, Science **342**, 1502 (2013).
[26] V. L. Deringer, C. J. Pickard, and G. Csányi, Data-Driven Learning of Total and Local Energies in Elemental Boron, Phys. Rev. Lett. **120**, 156001 (2018).
[27] E. V. Podryabinkin, E. V. Tikhonov, A. V. Shapeev, and A. R. Oganov, Accelerating crystal structure prediction by machine-learning interatomic potentials with active learning, Phys. Rev. B **99**, 064114 (2019).
[28] K. Gubaev, E. V. Podryabinkin, G. L. Hart, and A. V. Shapeev, Accelerating high-throughput searches for new alloys with active learning of interatomic potentials, Comput. Mater. Sci. **156**, 148 (2019).
[29] S. Kharabadze, A. Thorn, E. A. Koulakova, and A. N. Kolmogorov, Prediction of stable Li-Sn compounds: boosting ab initio searches with neural network potentials, npj Comput. Mater. **8**, 136 (2022).
[30] C. J. Pickard, Ephemeral data derived potentials for random structure search, Phys. Rev. B **106**, 014102 (2022).
[31] H. Wakai, A. Seko, and I. Tanaka, Efficient global crystal structure prediction using polynomial machine learning potential in the binary Al–Cu alloy system, J. Ceram. Soc. Jpn. **131**, 762 (2023).
[32] X. Dong and C. Fan, Rich stoichiometries of stable Ca-Bi system: Structure prediction and superconductivity, Sci. Rep. **5**, 9326 (2015).
[33] R. Li, Q. Xie, X. Cheng, D. Li, Y. Li, and X.-Q. Chen, First-principles study of the large-gap three-dimensional topological insulators M_3Bi_2 (M = Ca, Sr, Ba), Phys. Rev. B **92**, 205130 (2015).
[34] Z. K. Liu, B. Zhou, Y. Zhang, Z. J. Wang, H. M. Weng, D. Prabhakaran, S.-K. Mo, Z. X. Shen, Z. Fang, X. Dai, Z. Hussain, and Y. L. Chen, Discovery of a Three-Dimensional Topological Dirac Semimetal, Na_3Bi, Science **343**, 864 (2014).
[35] Z. Wang, Y. Sun, X.-Q. Chen, C. Franchini, G. Xu, H. Weng, X. Dai, and Z. Fang, Dirac semimetal and topological phase transitions in A_3Bi (A = Na, K, Rb), Phys. Rev. B **85**, 195320 (2012).
[36] R. Li, X. Cheng, Q. Xie, Y. Sun, D. Li, Y. Li, and X.-Q. Chen, Topological Metal of NaBi with Ultralow Lattice Thermal Conductivity and Electron-phonon Superconductivity, Sci. Rep. **5**, 8446 (2015).
[37] S. Sun, K. Liu, and H. Lei, Type-I superconductivity in KBi_2 single crystals, J. Phys. Condens. Matter **28**, 085701 (2016).
[38] M. Sturza, F. Han, C. D. Malliakas, D. Y. Chung, H. Claus, and M. G. Kanatzidis, Superconductivity in the intermetallic pnictide compound $Ca_{11}Bi_{10-x}$, Phys. Rev. B **89**, 054512 (2014).
[39] M. J. Winiarski, B. Wiendlocha, S. Gołąb, S. K. Kushwaha, P. Wiśniewski, D. Kaczorowski, J. D. Thompson, R. J. Cava, and T. Klimczuk, Superconductivity in $CaBi_2$, Phys. Chem. Chem. Phys. **18**, 21737 (2016).
[40] D. F. Shao, X. Luo, W. J. Lu, L. Hu, X. D. Zhu, W. H. Song, X. B. Zhu, and Y. P. Sun, Spin-orbit coupling enhanced superconductivity in Bi-rich compounds ABi_3 (A = Sr and Ba), Sci. Rep. **6**, 21484 (2016).
[41] A. Iyo, Y. Yanagi, S. Ishida, K. Oka, Y. Yoshida, K. Kihou, C. H. Lee, H. Kito, N. Takeshita, I. Hase, T. Yanagisawa, T. Kinjo, T. Nishio, and H. Eisaki, Superconductivity at 4.4 K in Ba_2Bi_3, Supercond. Sci. Technol. **27**,

072001 (2014).
[42] N. Haldolaarachchige, S. K. Kushwaha, Q. Gibson, and R. J. Cava, Superconducting properties of $BaBi_3$, Supercond. Sci. Technol. **27**, 105001 (2014).
[43] F. F. Tafti, M. S. Torikachvili, R. L. Stillwell, B. Baer, E. Stavrou, S. T. Weir, Y. K. Vohra, H.-Y. Yang, E. F. McDonnell, S. K. Kushwaha, Q. D. Gibson, R. J. Cava, and J. R. Jeffries, Tuning the electronic and the crystalline structure of LaBi by pressure: From extreme magnetoresistance to superconductivity, Phys. Rev. B **95**, 014507 (2017).
[44] C. Q. Xu, B. Li, M. R. van Delft, W. H. Jiao, W. Zhou, B. Qian, N. D. Zhigadlo, D. Qian, R. Sankar, N. E. Hussey, and X. Xu, Extreme magnetoresistance and pressure-induced superconductivity in the topological semimetal candidate YBi, Phys. Rev. B **99**, 024110 (2019).
[45] T. Kinjo, S. Kajino, T. Nishio, K. Kawashima, Y. Yanagi, I. Hase, T. Yanagisawa, S. Ishida, H. Kito, N. Takeshita, K. Oka, H. Eisaki, Y. Yoshida, and A. Iyo, Superconductivity in $LaBi_3$ with $AuCu_3$-type structure, Supercond. Sci. Technol. **29**, 03LT02 (2016).
[46] G. Dwari, S. Sasmal, S. Dan, B. Maity, V. Saini, R. Kulkarni, S. Banik, R. Verma, B. Singh, and A. Thamizhavel, Large unsaturated magnetoresistance and electronic structure studies of single-crystal GdBi, Phys. Rev. B **107**, 235117 (2023).
[47] A. Seko, Machine learning potentials for multicomponent systems: The Ti-Al binary system, Phys. Rev. B **102**, 174104 (2020).
[48] A. Seko, Tutorial: Systematic development of polynomial machine learning potentials for elemental and alloy systems, J. Appl. Phys. **133**, 011101 (2023).
[49] A. Seko, Polynomial machine learning potential and its application to global structure search in the ternary Cu-Ag-Au alloy (2024), arXiv:2407.20630 [cond-mat.mtrl-sci].
[50] A. Seko, Globally stable and metastable crystal structure enumeration using polynomial machine learning potentials for elemental As, Bi, Ga, In, La, P, Sb, Sn, and Te, Phys. Rev. B **110**, 224102 (2024).
[51] H. Wakai, A. Seko, and I. Tanaka, Global structure searches under varying temperatures and pressures using polynomial machine learning potentials: A case study on silicon (2025), arXiv:2503.22596 [cond-mat.mtrl-sci].
[52] A. Takahashi, A. Seko, and I. Tanaka, Conceptual and practical bases for the high accuracy of machine learning interatomic potentials: Application to elemental titanium, Phys. Rev. Mater. **1**, 063801 (2017).
[53] M. S. Daw and M. I. Baskes, Embedded-atom method: Derivation and application to impurities, surfaces, and other defects in metals, Phys. Rev. B **29**, 6443 (1984).
[54] M. I. Baskes, Modified embedded-atom potentials for cubic materials and impurities, Phys. Rev. B **46**, 2727 (1992).
[55] A. Seko, A. Takahashi, and I. Tanaka, First-principles interatomic potentials for ten elemental metals via compressed sensing, Phys. Rev. B **92**, 054113 (2015).
[56] T. Nishiyama, A. Seko, and I. Tanaka, Application of machine learning potentials to predict grain boundary properties in fcc elemental metals, Phys. Rev. Mater. **4**, 123607 (2020).
[57] S. Fujii and A. Seko, Structure and lattice thermal conductivity of grain boundaries in silicon by using machine learning potential and molecular dynamics, Comput. Mater. Sci. **204**, 111137 (2022).
[58] H. Wakai, A. Seko, H. Izuta, T. Nishiyama, and I. Tanaka, Predictive power of polynomial machine learning potentials for liquid states in 22 elemental systems, Phys. Rev. B **109**, 214207 (2024).
[59] D. Zagorac, H. Müller, S. Ruehl, J. Zagorac, and S. Rehme, Recent developments in the Inorganic Crystal Structure Database: theoretical crystal structure data and related features, J. Appl. Crystallogr. **52**, 918 (2019).
[60] A. Seko, `https://github.com/sekocha/pypolymlp`.
[61] P. E. Blöchl, Projector augmented-wave method, Phys. Rev. B **50**, 17953 (1994).
[62] G. Kresse and D. Joubert, From ultrasoft pseudopotentials to the projector augmented-wave method, Phys. Rev. B **59**, 1758 (1999).
[63] J. P. Perdew, K. Burke, and M. Ernzerhof, Generalized Gradient Approximation Made Simple, Phys. Rev. Lett. **77**, 3865 (1996).
[64] G. Kresse and J. Hafner, Ab initio molecular dynamics for liquid metals, Phys. Rev. B **47**, 558 (1993).
[65] G. Kresse and J. Furthmüller, Efficient iterative schemes for ab initio total-energy calculations using a plane-wave basis set, Phys. Rev. B **54**, 11169 (1996).
[66] G. Kresse and J. Furthmüller, Efficiency of ab-initio total energy calculations for metals and semiconductors using a plane-wave basis set, Comput. Mater. Sci. **6**, 15 (1996).
[67] F. Glover and G. A. Kochenberger, *Handbook of Metaheuristics* (Springer New York, 2003).
[68] C. J. Pickard and R. J. Needs, High-pressure phases of silane, Phys. Rev. Lett. **97**, 045504 (2006).
[69] P. P. Ferreira, L. J. Conway, A. Cucciari, S. Di Cataldo, F. Giannessi, E. Kogler, L. T. F. Eleno, C. J. Pickard, C. Heil, and L. Boeri, Search for ambient superconductivity in the Lu-N-H system, Nat. Commun. **14**, 5367 (2023).
[70] K. Dolui, L. J. Conway, C. Heil, T. A. Strobel, R. P. Prasankumar, and C. J. Pickard, Feasible route to high-temperature ambient-pressure hydride superconductivity, Phys. Rev. Lett. **132**, 166001 (2024).
[71] H. Wakai, `https://github.com/hytwakai/rsspolymlp`.
[72] IUCr, *International Tables for Crystallography, Volume A: Space Group Symmetry*, 5th ed., International Tables for Crystallography (Kluwer Academic Publishers, Dordrecht, Boston, London, 2002).
[73] P. Vinet, J. R. Smith, J. Ferrante, and J. H. Rose, Temperature effects on the universal equation of state of solids, Phys. Rev. B **35**, 1945 (1987).
[74] A. Togo, K. Shinohara, and I. Tanaka, Spglib: a software library for crystal symmetry search, Sci. Technol. Adv. Mater. Methods **4**, 2384822 (2024).
[75] K. Momma and F. Izumi, *VESTA3* for three-dimensional visualization of crystal, volumetric and morphology data, J. Appl. Crystallogr. **44**, 1272 (2011).
[76] G. Brauer and E. Zintl, Konstitution von Phosphiden, Arseniden, Antimoniden und Wismutiden des Lithiums, Natriums und Kaliums, Z. Phys. Chem. **37B**, 323 (1937).
[77] E. Zintl and W. Dullenkopf, Polyantimonide, Polywismutide und ihr Übergang in Legierungen, Z. Phys.

Chem. **16B**, 183 (1932).
[78] F. Emmerling, N. Längin, D. Petri, M. Kroeker, and C. Röhr, Alkalimetallbismutide ABi und ABi_2 (A = K, Rb, Cs) — Synthesen, Kristallstrukturen, Eigenschaften, Z. Anorg. Allg. Chem. **630**, 171 (2004).
[79] H. Kerber, H.-J. Deiseroth, and R. Walther, Crystal structure of α-tripotassium bismuthide, α-K_3Bi, a revision, Z. Kristallogr. - New Cryst. Struct. **213**, 501 (1998).
[80] D. E. Sands, D. H. Woods, and W. J. Ramsey, The crystal structure of β-K_3Bi, Acta Crystallogr. **16**, 316 (1963).
[81] E. Zintl and E. Husemann, Bindungsart und Gitterbau binärer Magnesiumverbindungen, Z. Phys. Chem. **21B**, 138 (1933).
[82] M. Calderón-Cueva, W. Peng, S. M. Clarke, J. Ding, B. L. Brugman, G. Levental, A. Balodhi, M. Rylko, O. Delaire, J. P. S. Walsh, S. M. Dorfman, and A. Zevalkink, Anisotropic Structural Collapse of Mg_3Sb_2 and Mg_3Bi_2 at High Pressure, Chem. Mater. **33**, 567 (2021).
[83] B. Eisenmann and H. Schäfer, Die Kristallstrukturen der Verbindungen Ca_2Sb und Ca_2Bi / The Crystal Structures of Ca_2Sb and Ca_2Bi, Z. Naturforsch., B **29**, 13 (1974).
[84] K. Deller and B. Eisenmann, Zur Kenntnis von $Ca_{11}Sb_{10}$ und $Ca_{11}Bi_{10}$, Z. Naturforsch., B **31**, 29 (1976).
[85] F. Merlo and M. Fornasini, Crystal structure of some phases and alloying behaviour in alkaline earths, europium and ytterbium pnictides, Mater. Res. Bull. **29**, 149 (1994).
[86] M. Martinez-Ripoll, A. Haase, and G. Brauer, The crystal structure of Ca_5Bi_3, Acta Crystallogr., Sect. B **30**, 2004 (1974).
[87] N. Zhuravlev and V. M. Adamyan, Study of the crystal structure of the superconducting compounds $SrBi_3$ and $BaBi_3$, Sov. Phys. Crystallogr. **6**, 121 (1961).
[88] B. Eisenmann and K. Deller, Zur Kenntnis der Erdalkaliantimonide und -wismutide Sr_2Bi, Ba_2Sb, Sr_5Bi_3, Ba_5Sb_3 und Ba_5Bi_3 / On the Earth-Alkali-Antimonides and Bismutides Sr_2Bi, Ba_2Sb, Sr_5Bi_3, Ba_5Sb_3 and Ba_5Bi_3, Z. Naturforsch., B **30**, 66 (1975).
[89] W. M. Hurng and J. D. Corbett, Alkaline-earth-metal antimonides and bismuthides with the A_5Pn_3 stoichiometry. Interstitial and other Zintl phases formed on their reactions with halogen or sulfur, Chem. Mater. **1**, 311 (1989).
[90] G. Bruzzone, E. Franceschi, and F. Merlo, M_5X_3 intermediate phases formed by Ca, Sr and Ba, J. Less Common Met. **60**, 59 (1978).
[91] S. Ponou and T. F. Fässler, Nonclassical Bonding in the Novel Structure of Ba_2Bi_3 and Unexpected Site Preference in the Coloring Variant Ba_2BiSb_3, Inorg. Chem. **43**, 6124 (2004).
[92] M. Martinez-Ripoll, A. Haase, and G. Brauer, The crystal structure of Ba_2Bi, Acta Crystallogr., Sect. B **30**, 2003 (1974).
[93] B. Li, A.-V. Mudring, and J. D. Corbett, Valence Compounds versus Metals. Synthesis, Characterization, and Electronic Structures of Cubic Ae_4Pn_3 Phases in the Systems Ae = Ca, Sr, Ba, Eu; Pn = As, Sb, Bi, Inorg. Chem. **42**, 6940 (2003).
[94] G. Derrien, M. Tillard-Charbonnel, A. Manteghetti, L. Monconduit, and C. Belin, Synthesis and Crystal Structure of $M_{11}X_{10}$ Compounds, M=Sr, Ba and X=Bi, Sb. Electronic Requirements and Chemical Bonding, J. Solid State Chem. **164**, 169 (2002).
[95] M. G. Haase, H. Block, and W. Jeitschko, Preparation and Crystal Structures of some Binary Pnictides of Scandium, Zirconium, and Hafnium: Sc_5Bi_3, ZrBi, α-HfSb, HfBi, $HfBi_2$, and the Compound $Zr_5Bi_3X_{1\check{}x}$, Possibly Stabilized by an Impurity (X), Zeitschrift für anorganische und allgemeine Chemie **627**, 1941 (2001).
[96] N. Zhuravlev and E. Smirnova, Alloys of bismuth and antimony with scandium, Sov. Phys. Crystallogr. **7** (1962).
[97] F. Schmidt, O. McMasters, and R. Lichtenberg, The yttrium-bismuth alloy system, J. Less Common Met. **18**, 215 (1969).
[98] B. C. Wang, E. J. Gabe, L. D. Calvert, and J. B. Taylor, The crystal structure of Y_5Bi_3 and its relation to the Mn_5Si_3 and the Yb_5Sb_3 type structures, Acta Crystallogr., Sect. B **32**, 1440 (1976).
[99] K. Yoshihara, J. Taylor, L. Calvert, and J. Despault, Rare-earth bismuthides, J. Less Common Met. **41**, 329 (1975).
[100] E. A. Leon-Escamilla and J. D. Corbett, Hydrogen in Polar Intermetallics. Binary Pnictides of Divalent Metals with Mn_5Si_3-type Structures and Their Isotypic Ternary Hydride Solutions, Chem. Mater. **18**, 4782 (2006).
[101] R. Gambino, Rare-earth-Sb and -Bi compounds with the Gd_4Bi_3 (anti-Th_3P_4) structure, J. Less Common Met. **12**, 344 (1967).
[102] J. B. Taylor, L. D. Calvert, and Y. Wang, Powder data for some new europium antimonides and bismuthides, J. Appl. Crystallogr. **12**, 249 (1979).
[103] Z.-M. Sun and J.-G. Mao, Synthesis and crystal structure of $EuBi_2$, J. Solid State Chem. **177**, 3752 (2004).
[104] A. Nakamura, Y. Hiranaka, M. Hedo, T. Nakama, Y. Tatetsu, T. Maehira, Y. Miura, A. Mori, H. Tsutsumi, Y. Hirose, K. Mitamura, K. Sugiyama, M. Hagiwara, F. Honda, T. Takeuchi, Y. Haga, K. Matsubayashi, Y. Uwatoko, and Y. Ōnuki, Fermi Surface and Magnetic Properties of Antiferromagnet $EuBi_3$, J. Phys. Soc. Jpn. **82**, 124708 (2013).
[105] D. Hohnke and E. Parthé, Rare-earth bismuthides with $D8_8$ and Hf_5Sn_3Cu-type structures, J. Less Common Met. **17**, 291 (1969).
[106] D. Hohnke and E. Parthé, The anti-Th_3P_4 structure type for rare earth germanides, antimonides and bismuthides, Acta Crystallogr. **21**, 435 (1966).
[107] M. Drzyzga and J. Szade, Structure and magnetism of R_5Bi_3 (R=Tb, Dy, Ho, Er) and Tb_4Bi_3, J. Alloys Compd. **321**, 27 (2001).

Supplemental Material: Systematic global structure search of bismuth-based binary systems under pressure using machine learning potentials

Hayato Wakai,[1,*] Shintaro Ishiwata,[2,3] and Atsuto Seko[1,†]

[1] *Department of Materials Science and Engineering, Kyoto University, Kyoto 606-8501, Japan*
[2] *Division of Materials Physics and Center for Spintronics Research Network (CSRN), Graduate School of Engineering Science, The University of Osaka, Toyonaka, Osaka 560-8531, Japan*
[3] *Spintronics Research Network Division, Institute for Open and Transdisciplinary Research Initiatives, The University of Osaka, Suita, Osaka 565-0871, Japan*

(Dated: November 10, 2025)

A. Global minimum structures of the endmembers

Table I summarizes the global minimum structures of the endmembers within the pressure range of 0–20 GPa. In the following, we discuss the predicted structures in more detail.

1. *Na and K*

For alkali metals, the body-centered cubic (BCC) structure has been reported to be stable up to 65 GPa in elemental Na, while in elemental K the BCC structure has been reported to transform into the face-centered cubic (FCC) structure at 11.6 GPa [1]. Although these structures are identified as global minima in this study, the α–La-type structure in elemental Na and the hexagonal close-packed (HCP) structure in elemental K, neither of which has been experimentally reported, are also computed as global minima around 0–1 GPa. In this pressure range, many

TABLE I. Predicted global minimum structures of the endmembers. These structures are predicted to be stable within the pressure ranges (in GPa) indicated in the "Pressure" column. Z denotes the number of atoms in the unit cell. The "ICSD-ID" column lists the corresponding identifiers in the ICSD. The "Prototype" column indicates known prototype structures adopted by the predicted structures. Structures reported in the ICSD but not obtained through RSS are indicated by parentheses in the "Pressure" column.

Formula	Space group	Z	ICSD-ID	Prototype	Pressure	Formula	Space group	Z	ICSD-ID	Prototype	Pressure
Bi	$R\bar{3}m$	6	241983	Bi-I (A7)	(0.0–3.0)	Sc	$P6_3/mmc$	2	102654	HCP (A3)	0.0–13.6
	$P4/ncc$	32	—	Bi-III	(3.0–8.1)		$I4/mcm$	32	—	—	13.6–20.0
	$I4_1/acd$	32	—	—	8.1–13.8	Y	$P6_3/mmc$	2	196971	HCP (A3)	0.0–1.1
	$Im\bar{3}m$	2	52725	Bi-V (A2)	13.8–20.0		$R\bar{3}m$	9	—	α–Sm (C19)	1.1–9.3
Na	$P6_3/mmc$	4	—	α–La (A3′)	0.0–1.5		$R\bar{3}m$	21	—	—	9.3–9.6
	$Im\bar{3}m$	2	196972	BCC (A2)	1.5–20.0		$P6_3/mmc$	4	—	α–La (A3′)	9.6–20.0
K	$P6_3/mmc$	2	—	HCP (A3)	0.0–0.1	La	$P6_3/mmc$	4	102655	α–La (A3′)	0.0–0.4
	$Im\bar{3}m$	2	196973	BCC (A2)	0.1–11.9		$R\bar{3}m$	15	—	—	0.4–4.9
	$Fm\bar{3}m$	4	44669	FCC (A1)	11.9–20.0		$R\bar{3}m$	24	—	—	4.9–20.0
Mg	$P6_3/mmc$	2	166868	HCP (A3)	0.0–20.0	Eu	$Im\bar{3}m$	2	102658	BCC (A2)	0.0–10.0
Ca	$Fm\bar{3}m$	4	126372	FCC (A1)	0.0–7.6		$P6_3/mmc$	2	53423	HCP (A3)	10.0–15.6
	$Im\bar{3}m$	2	189147	BCC (A2)	7.6–20.0		$C2/c$	12	—	—	15.6–19.6
Sr	$Fm\bar{3}m$	4	198199	FCC (A1)	0.0–1.0		$C2$	22	—	—	19.6–20.0
	$Im\bar{3}m$	2	198197	BCC (A2)	1.0–20.0	Gd	$P6_3/mmc$	4	53607	α–La (A3′)	0.0–20.0
Ba	$Im\bar{3}m$	2	108091	BCC (A2)	0.0–3.8						
	$P6_3/mmc$	2	52680	HCP (A3)	3.8–20.0						

* wakai@cms.mtl.kyoto-u.ac.jp
† seko@cms.mtl.kyoto-u.ac.jp

structures, including the BCC, FCC, HCP, α–Sm-type, and α–La-type structures, exhibit nearly identical enthalpies in these systems.

2. Mg, Ca, Sr, and Ba

For alkaline-earth metal Mg, the HCP structure is computed as the global minimum over the entire pressure range of 0–20 GPa, consistent with the experimental report [2]. The elemental Ca and Sr crystallize in the FCC structure under ambient conditions and transform into the BCC structure at 20 and 3.5 GPa, respectively, as reported experimentally [1]. These phases are predicted to be global minima, and the phase transition sequence is consistent with the results obtained in this study. In elemental Ba, the BCC structure has been experimentally reported to transform into the HCP structure at 5.5 GPa, and the HCP structure to transform into a host–guest structure at 12 GPa [1]. In the present structure search, the BCC and HCP structures are identified as global minima.

3. Sc, Y, and La

For elemental Sc, the HCP structure has been reported to be stable up to 23 GPa, and it transforms into a host–guest structure above this pressure [3]. In this study, the HCP structure is computed to be the global minimum at low pressures, and a global minimum with space group $I4/mcm$ is found at higher pressures. The structure with space group $I4/mcm$ is regarded as being consistent with the experimentally reported host–guest structure when the simplest structural model representing the host–guest arrangement is applied [3]. This $I4/mcm$ structure has also been identified in a DFT-based global structure search reported in the literature [4].

In elemental Y, the HCP structure has been reported to be stable under ambient conditions, to transform into the α–Sm-type structure at 10–15 GPa, and to subsequently transform into the α–La-type structure at 25–28 GPa [2]. These structures are obtained in the current structure search, and an experimentally unreported structure with space group $R\bar{3}m$ is also identified. Although the transition pressures computed in this study are lower than those experimentally reported, the transition sequence agrees with the experimental results.

In elemental La, previous experimental studies have revealed that the α–La structure, stable at ambient pressure, transforms into FCC structure at approximately 2.2 GPa, subsequently changes to a distorted FCC structure with space group $R\bar{3}m$ at 5.4 GPa, and reverts to the FCC structure at 53 GPa [5, 6]. All of these structures are reproduced in the present global structure search. The experimentally reported distorted FCC structure corresponds to the global minimum with space group $R\bar{3}m$ containing 24 atoms. However, the FCC structure is predicted to be metastable at 0–20 GPa, which is inconsistent with the experimental observation at 2.2–5.4 GPa. Instead, a global minimum with space group $R\bar{3}m$ containing 15 atoms is identified in the current search. Its enthalpy is nearly identical to that of the FCC structure, particularly in the pressure range of 2–4 GPa.

4. Eu and Gd

The rare-earth metal Eu adopts the BCC structure at ambient pressure, transforms into the HCP structure at 12 GPa, and further transforms into an incommensurately modulated monoclinic structure with space group $C2/c$ at 30 GPa, as reported in experimental studies [7, 8]. In this study, the BCC and HCP structures are computed as global minima, and additional global minima with space groups $C2/c$ and $C2$ are also obtained.

Experimental studies have shown that elemental Gd crystallizes in the HCP structure at ambient pressure, transforms into the α–Sm-type structure at 1.5 GPa, and subsequently transforms into the α–La-type structure at 5–7 GPa, which remains stable up to 24–29 GPa [9, 10]. In the present calculations, the α–La-type structure is predicted to be the global minimum throughout the pressure range of 0–20 GPa, while the HCP and α–Sm-type structures are obtained as metastable structures.

5. Bi

Experimental studies on elemental Bi have identified various distinct phases that appear sequentially with increasing pressure at room temperature within 0–20 GPa: Bi-I, Bi-Ⅱ, Bi-Ⅲ, and Bi-V [12–14]. The transition pressures between Bi-I and Bi-Ⅱ, between Bi-Ⅱ and Bi-Ⅲ, and between Bi-Ⅲ and Bi-V are 2.5, 2.7, and 8 GPa, respectively. Bi-Ⅲ is a host–guest structure requiring at least 32 atoms even using an approximate representation [15], and therefore lies outside the current search space. Consequently, the DFT calculation for this structure is performed using the

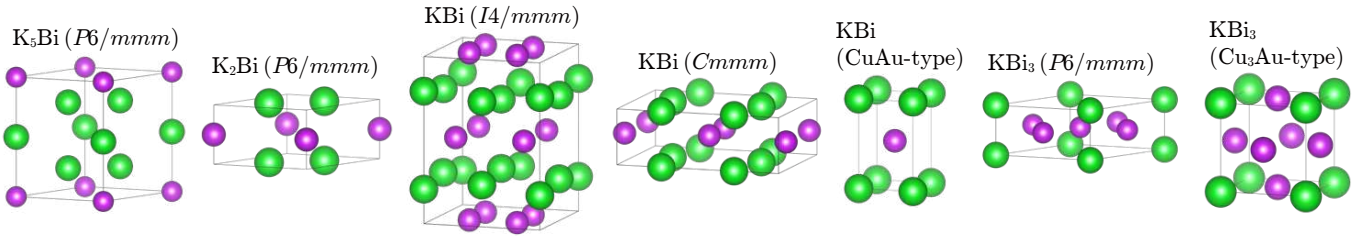

FIG. 1. Crystal structures of the thermodynamically stable compounds that have not been experimentally reported in the K–Bi system. Green and purple spheres represent K and Bi atoms, respectively. These structures are visualized using VESTA [11].

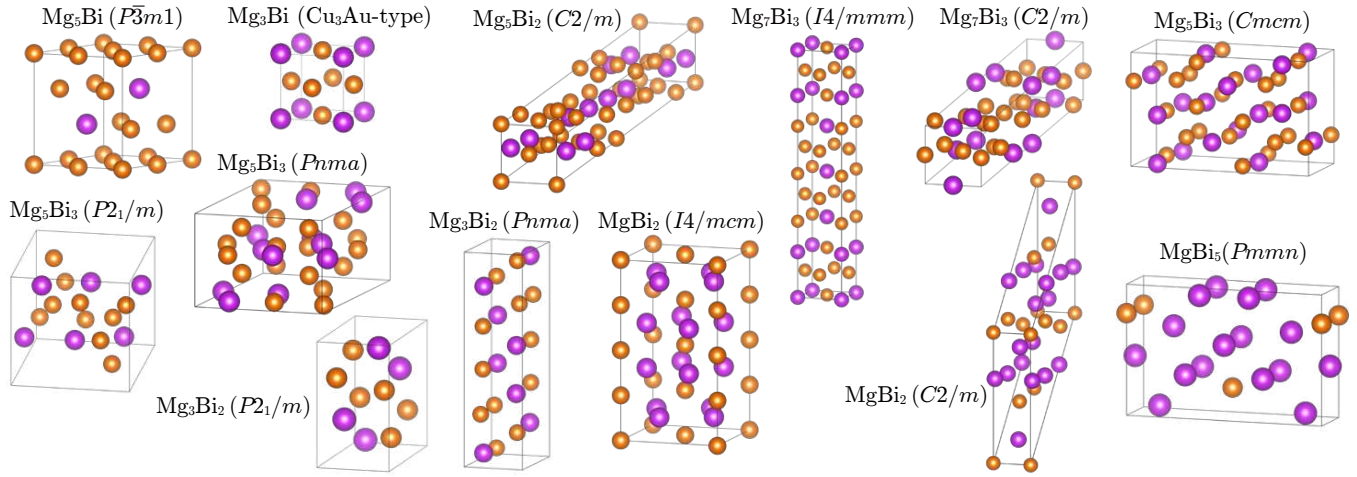

FIG. 2. Crystal structures of the thermodynamically stable compounds that have not been experimentally reported in the Mg–Bi system. Orange and purple spheres represent Mg and Bi atoms, respectively.

experimentally determined structure. As a result, in this study, a sequence of stable structures at zero temperature is predicted as Bi-I, Bi-Ⅲ, a structure with space group $I4_1/acd$, and Bi-V. On the other hand, Bi-II is predicted to be metastable.

In addition, the Bi-I structure is not obtained in the present search, although a structure with the space group $Imma$, which is similar to that of Bi-I, is identified. Both of these structures were also reported in the global structure search employing the polynomial MLP at zero pressure in Ref. [16]. Therefore, the predictive power of the current MLPs constructed for the Bi-based binary systems appears to be slightly lower for elemental Bi than that of the previous MLP developed exclusively for elemental Bi. Nevertheless, because the Bi-I and $Imma$ structures

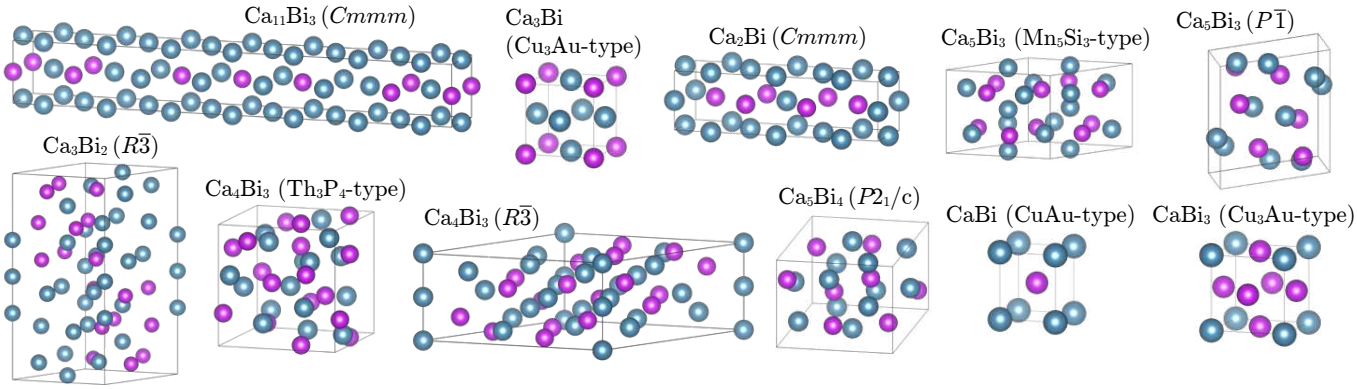

FIG. 3. Crystal structures of the thermodynamically stable compounds that have not been experimentally reported in the Ca–Bi system. Blue and purple spheres represent Ca and Bi atoms, respectively.

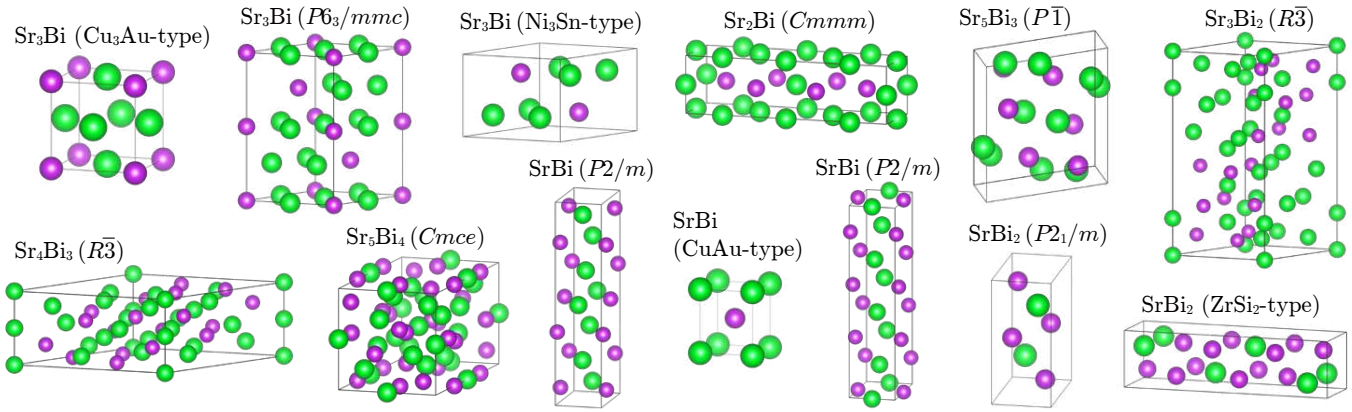

FIG. 4. Crystal structures of the thermodynamically stable compounds that have not been experimentally reported in the Sr–Bi system. Green and purple spheres represent Sr and Bi atoms, respectively.

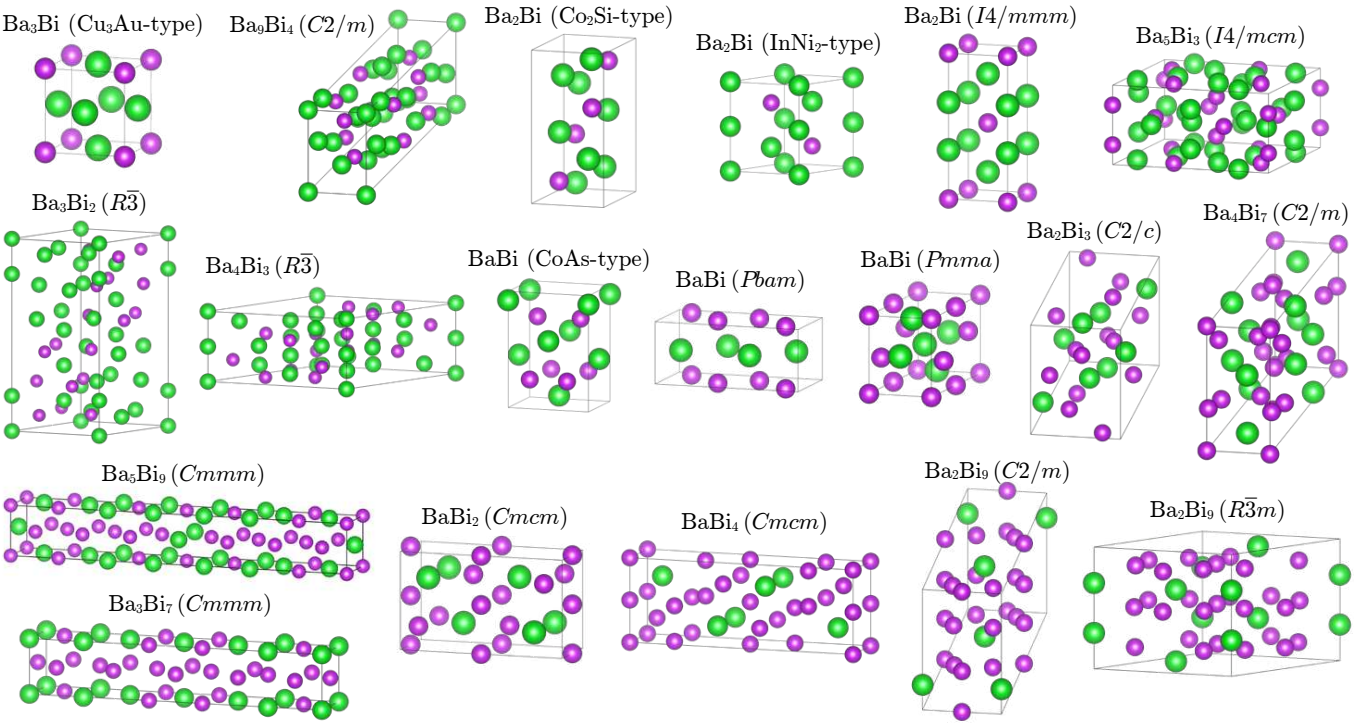

FIG. 5. Crystal structures of the thermodynamically stable compounds that have not been experimentally reported in the Ba–Bi system. Green and purple spheres represent Ba and Bi atoms, respectively.

have nearly identical enthalpies, the stability of the binary compounds predicted in this study is not affected by the reduced predictive accuracy for elemental Bi.

B. Visualization of thermodynamically stable structures

Figures 1–10 present the crystal structures of the thermodynamically stable compounds in the K–Bi, Mg–Bi, Ca–Bi, Sr–Bi, Ba–Bi, Sc–Bi, Y–Bi, La–Bi, Eu–Bi, and Gd–Bi systems.

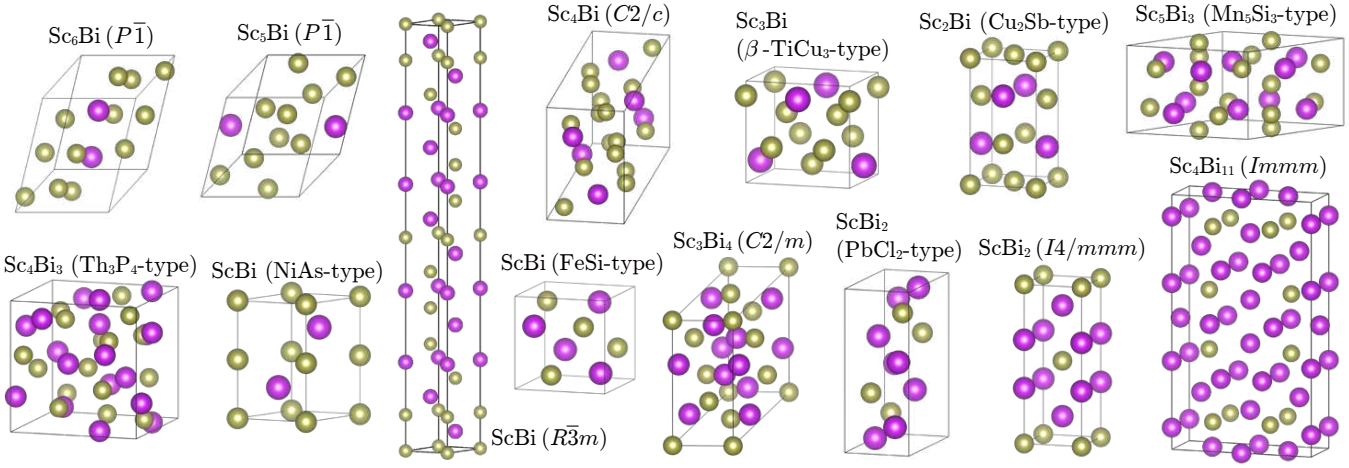

FIG. 6. Crystal structures of the thermodynamically stable compounds that have not been experimentally reported in the Sc–Bi system. Dark yellow and purple spheres represent Sc and Bi atoms, respectively.

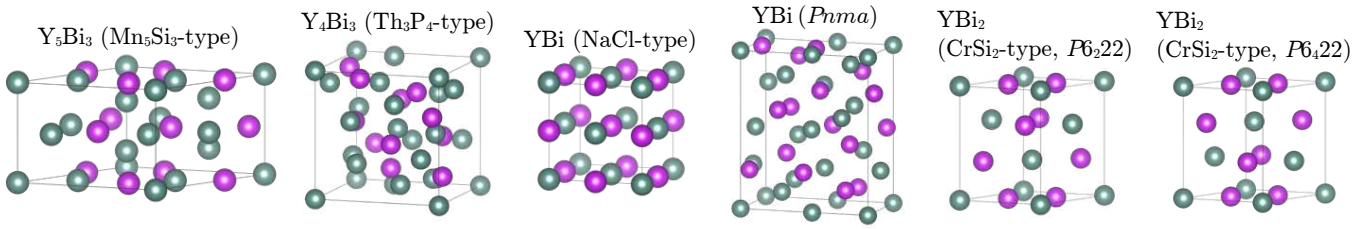

FIG. 7. Crystal structures of the thermodynamically stable compounds in the Y–Bi system. Gray and purple spheres represent Y and Bi atoms, respectively.

C. Formation enthalpies for local minimum structures obtained through RSS

Figures 11–20 show formation enthalpies calculated by the MLPs for local minimum structures in K–Bi, Mg–Bi, Ca–Bi, Sr–Bi, Ba–Bi, Sc–Bi, Y–Bi, La–Bi, Eu–Bi, and Gd–Bi, demonstrating that an enormous number of structures are identified across all compositions. In addition, the convex hulls computed by the MLPs closely match those computed by DFT, confirming that the combination of RSS and MLP enables accurate enumeration of local minimum structures.

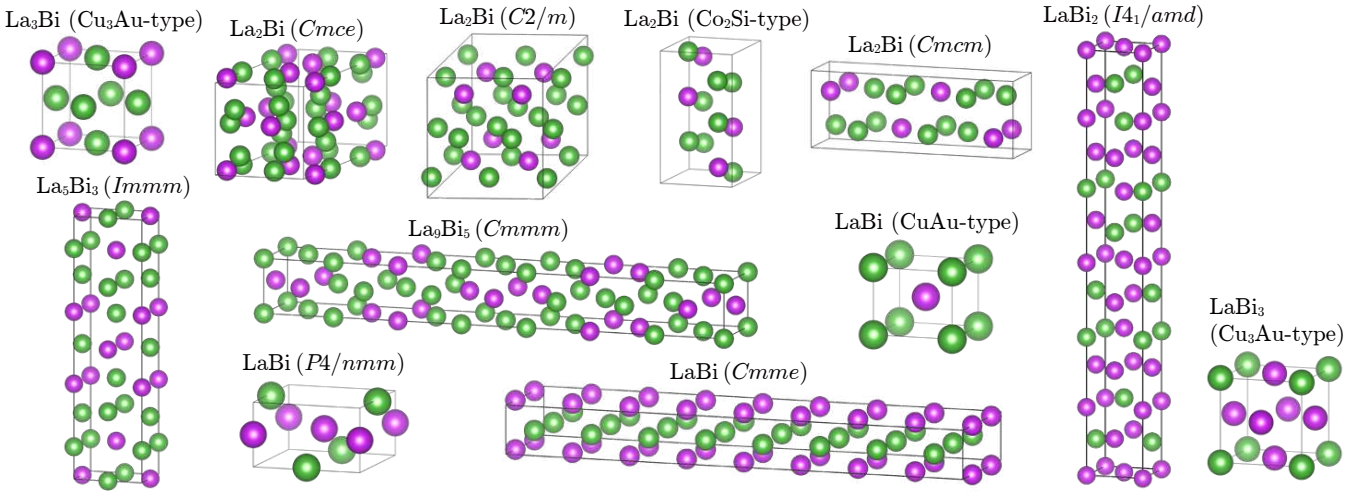

FIG. 8. Crystal structures of the thermodynamically stable compounds that have not been experimentally reported in the La–Bi system. Green and purple spheres represent La and Bi atoms, respectively.

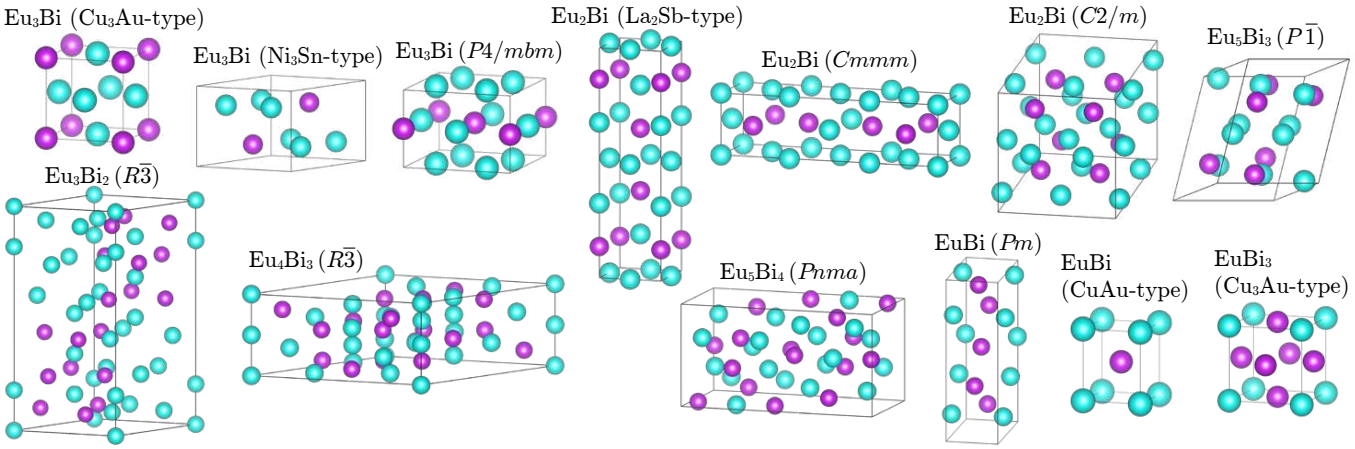

FIG. 9. Crystal structures of the thermodynamically stable compounds that have not been experimentally reported in the Eu–Bi system. Light blue and purple spheres represent Eu and Bi atoms, respectively.

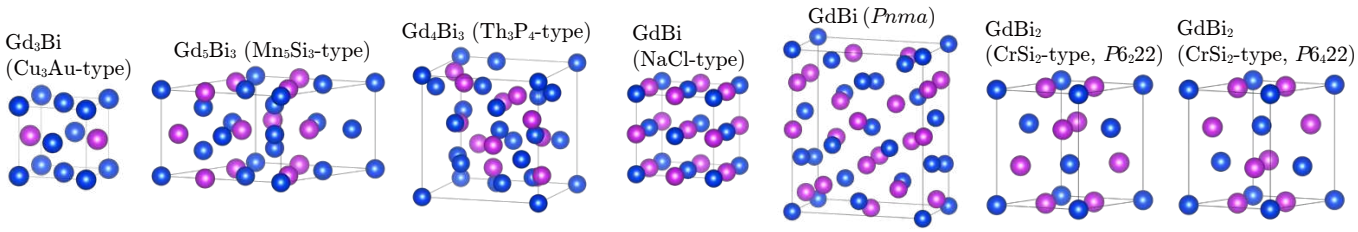

FIG. 10. Crystal structures of the thermodynamically stable compounds in the Gd–Bi system. Blue and purple spheres represent Gd and Bi atoms, respectively.

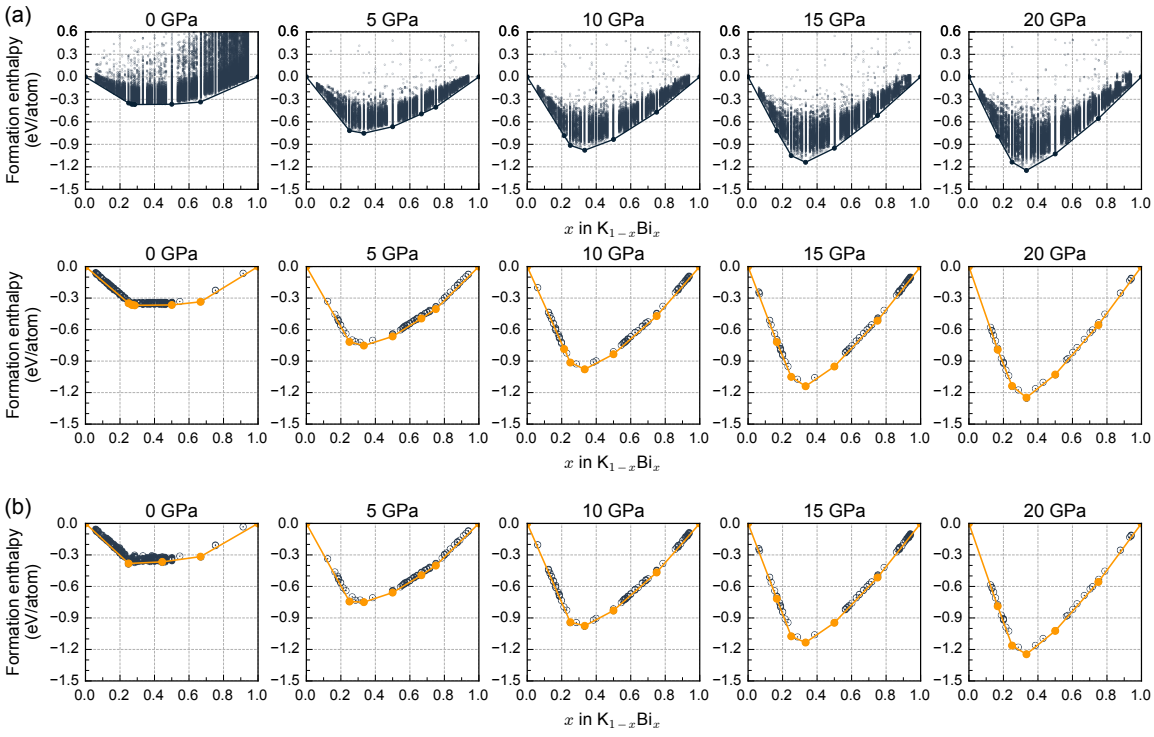

FIG. 11. (a) Formation enthalpies predicted using the MLP for local minimum structures generated with MLP-based RSS in the K–Bi system, shown in the upper panel. The lower panel presents the formation enthalpies of a subset of local minima with ΔH_{ch} values below 25 meV/atom. (b) Formation enthalpies calculated using DFT for the subset of structures shown in the lower panel of (a). These structures were fully optimized using DFT.

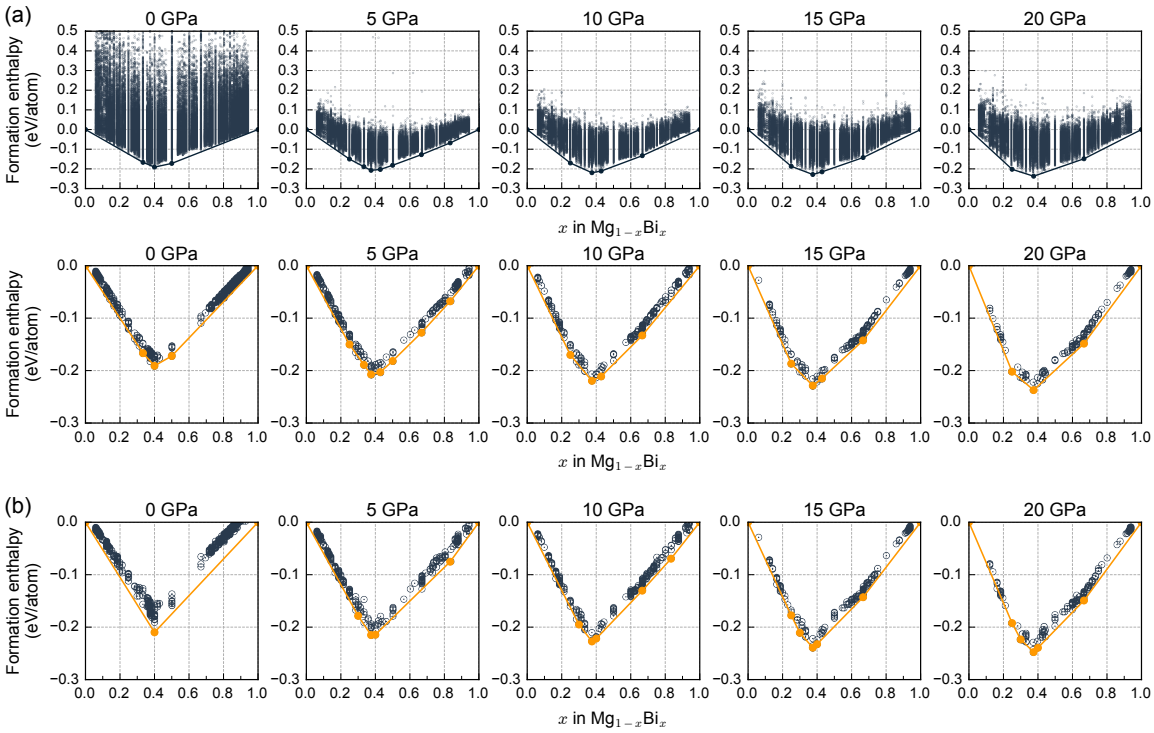

FIG. 12. (a) Formation enthalpies predicted using the MLP for local minimum structures generated with MLP-based RSS in the Mg–Bi system, shown in the upper panel. The lower panel presents the formation enthalpies of a subset of local minima with ΔH_{ch} values below 20 meV/atom. (b) Formation enthalpies calculated using DFT for the subset of structures shown in the lower panel of (a). These structures were fully optimized using DFT.

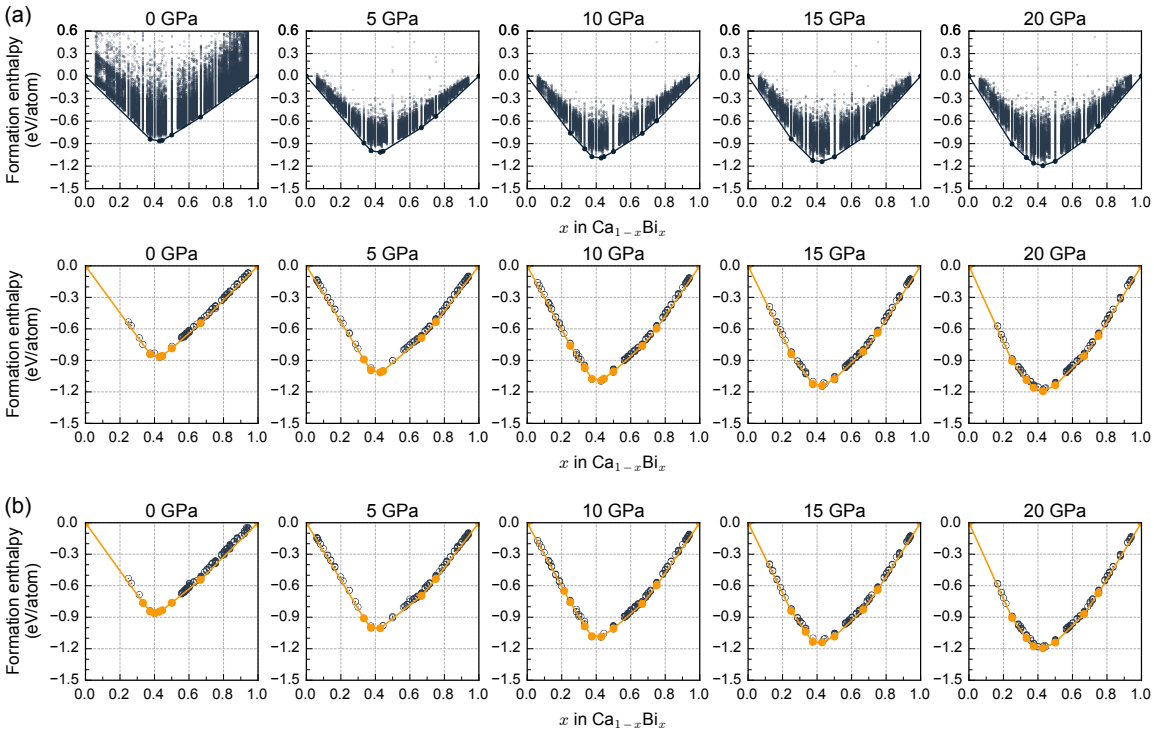

FIG. 13. (a) Formation enthalpies predicted using the MLP for local minimum structures generated with MLP-based RSS in the Ca–Bi system, shown in the upper panel. The lower panel presents the formation enthalpies of a subset of local minima with ΔH_{ch} values below 30 meV/atom. (b) Formation enthalpies calculated using DFT for the subset of structures shown in the lower panel of (a). These structures were fully optimized using DFT.

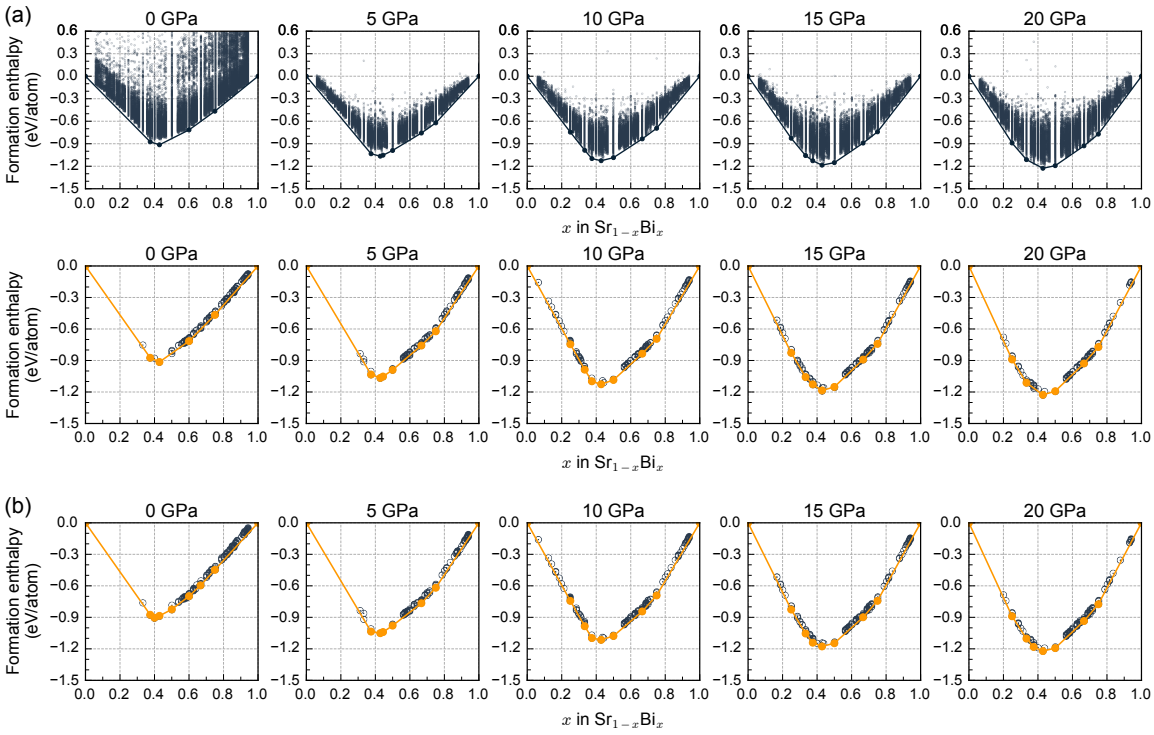

FIG. 14. (a) Formation enthalpies predicted using the MLP for local minimum structures generated with MLP-based RSS in the Sr–Bi system, shown in the upper panel. The lower panel presents the formation enthalpies of a subset of local minima with ΔH_{ch} values below 35 meV/atom. (b) Formation enthalpies calculated using DFT for the subset of structures shown in the lower panel of (a). These structures were fully optimized using DFT.

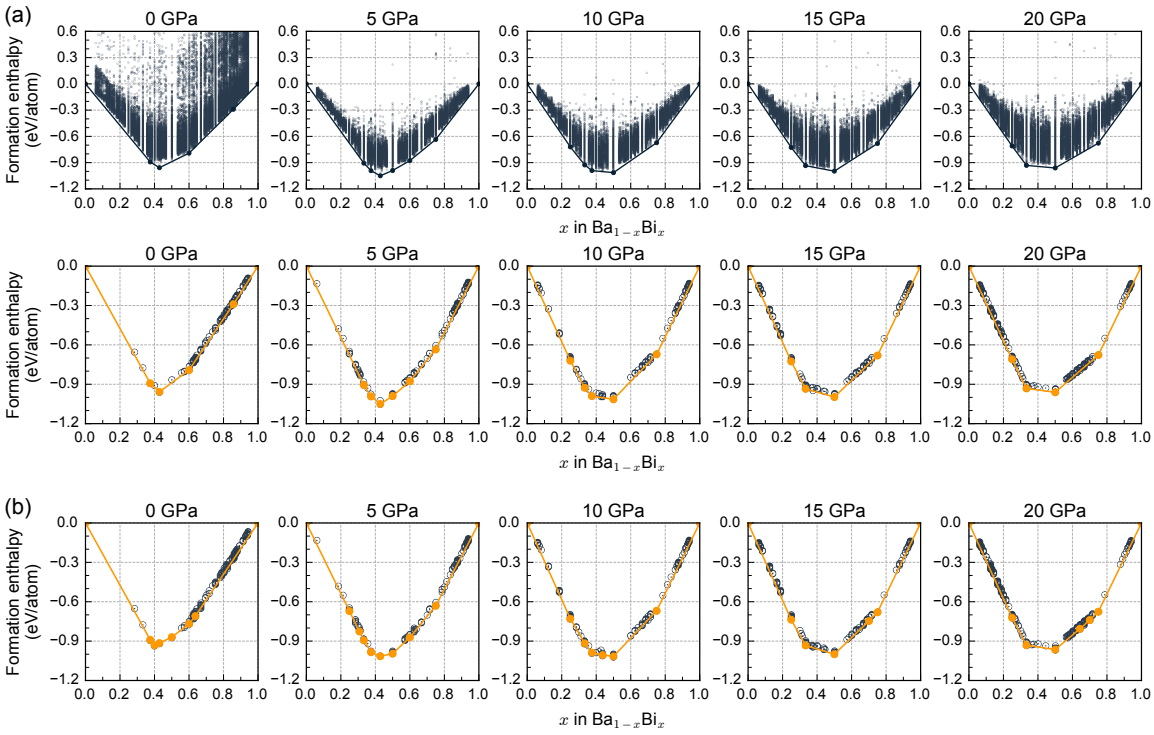

FIG. 15. (a) Formation enthalpies predicted using the MLP for local minimum structures generated with MLP-based RSS in the Ba–Bi system, shown in the upper panel. The lower panel presents the formation enthalpies of a subset of local minima with ΔH_{ch} values below 30 meV/atom. (b) Formation enthalpies calculated using DFT for the subset of structures shown in the lower panel of (a). These structures were fully optimized using DFT.

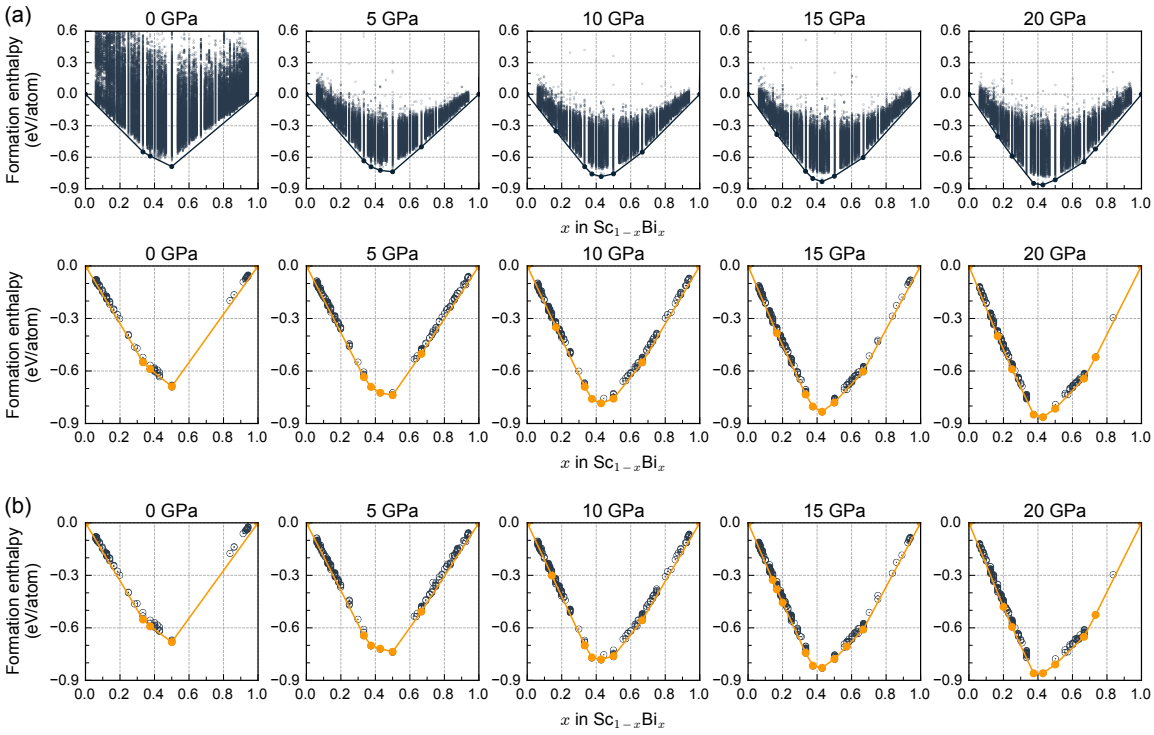

FIG. 16. (a) Formation enthalpies predicted using the MLP for local minimum structures generated with MLP-based RSS in the Sc–Bi system, shown in the upper panel. The lower panel presents the formation enthalpies of a subset of local minima with ΔH_{ch} values below 30 meV/atom. (b) Formation enthalpies calculated using DFT for the subset of structures shown in the lower panel of (a). These structures were fully optimized using DFT.

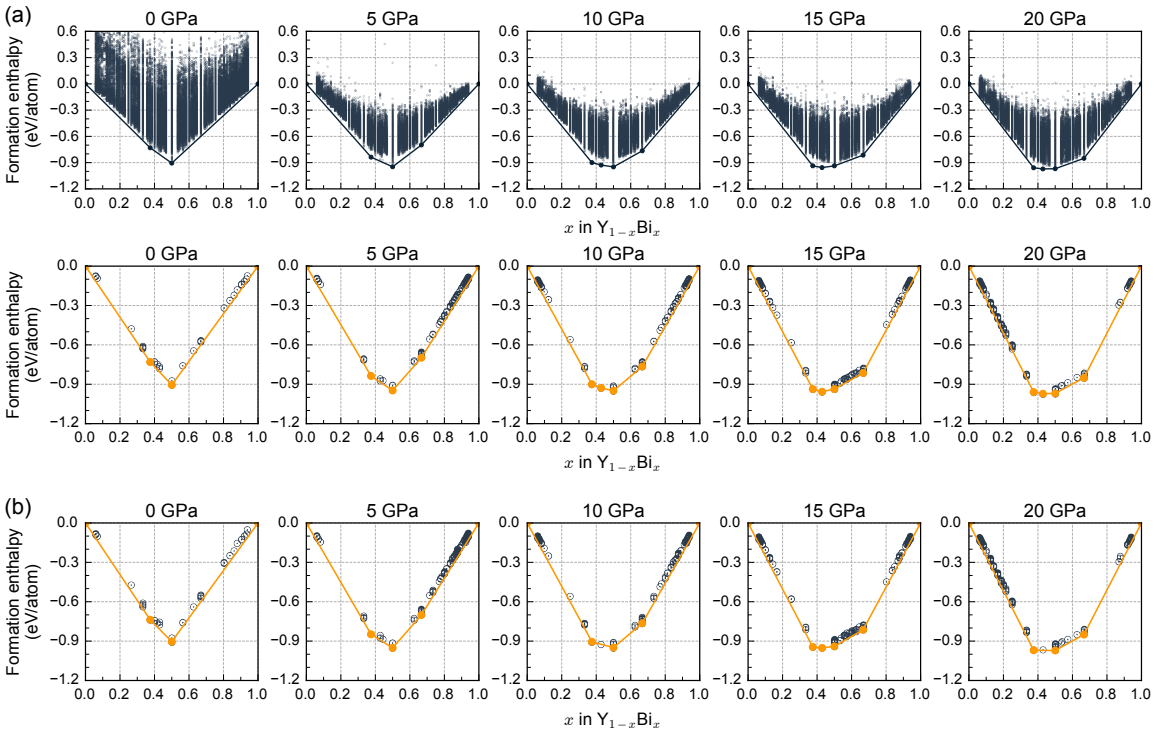

FIG. 17. (a) Formation enthalpies predicted using the MLP for local minimum structures generated with MLP-based RSS in the Y–Bi system, shown in the upper panel. The lower panel presents the formation enthalpies of a subset of local minima with ΔH_{ch} values below 40 meV/atom. (b) Formation enthalpies calculated using DFT for the subset of structures shown in the lower panel of (a). These structures were fully optimized using DFT.

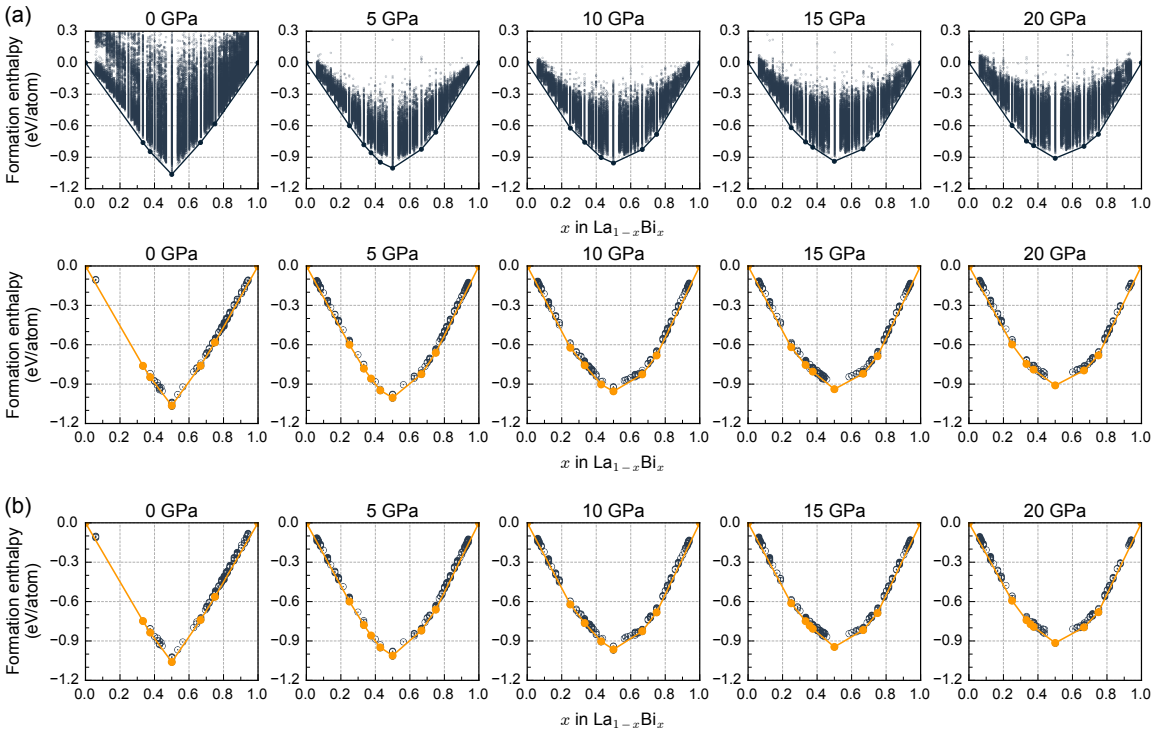

FIG. 18. (a) Formation enthalpies predicted using the MLP for local minimum structures generated with MLP-based RSS in the La–Bi system, shown in the upper panel. The lower panel presents the formation enthalpies of a subset of local minima with ΔH_{ch} values below 35 meV/atom. (b) Formation enthalpies calculated using DFT for the subset of structures shown in the lower panel of (a). These structures were fully optimized using DFT.

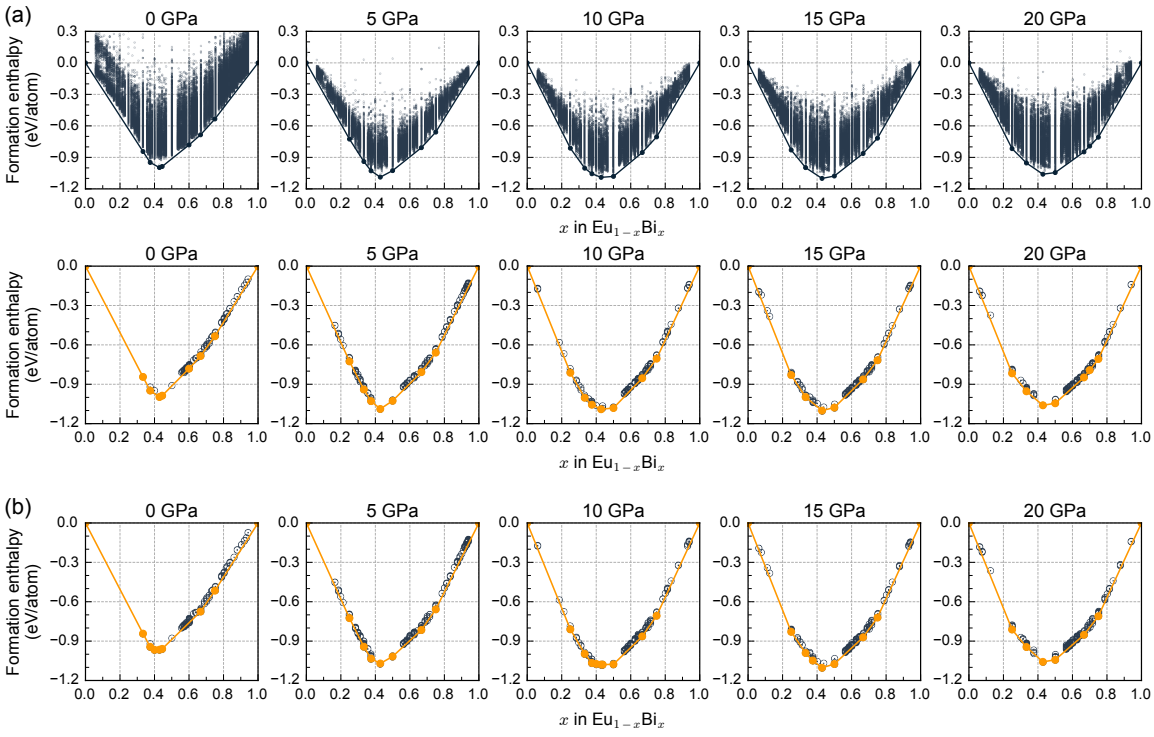

FIG. 19. (a) Formation enthalpies predicted using the MLP for local minimum structures generated with MLP-based RSS in the Eu–Bi system, shown in the upper panel. The lower panel presents the formation enthalpies of a subset of local minima with ΔH_{ch} values below 30 meV/atom. (b) Formation enthalpies calculated using DFT for the subset of structures shown in the lower panel of (a). These structures were fully optimized using DFT.

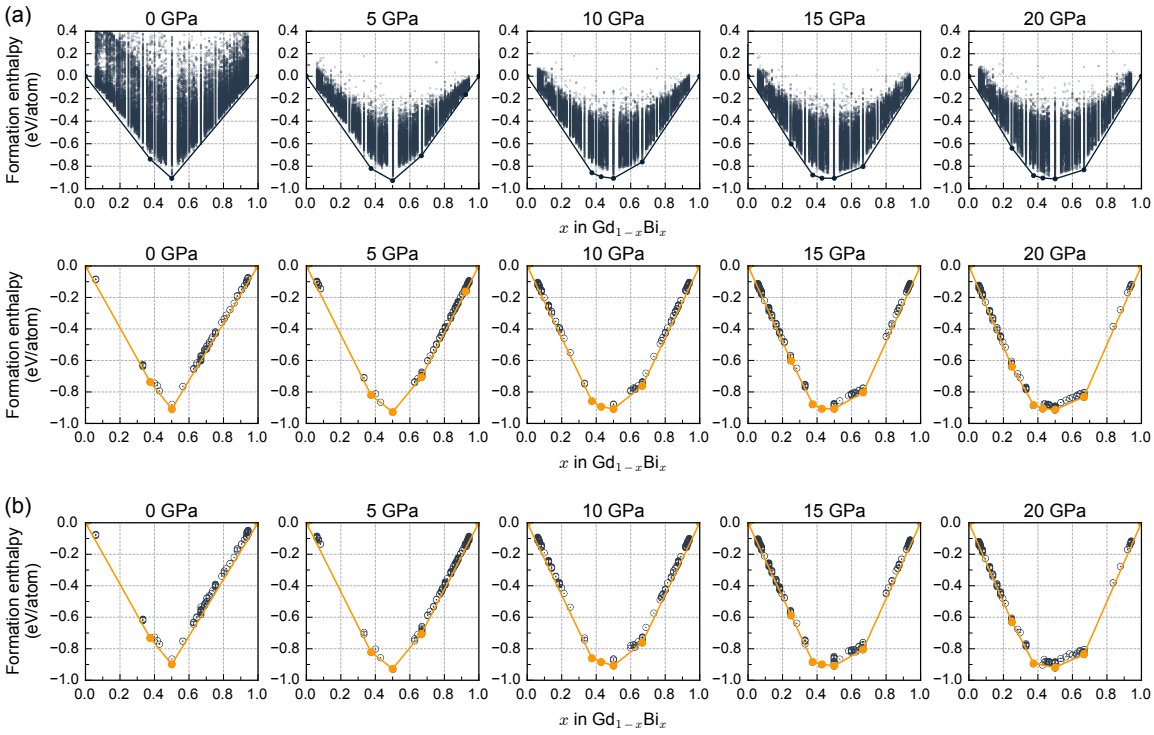

FIG. 20. (a) Formation enthalpies predicted using the MLP for local minimum structures generated with MLP-based RSS in the Gd–Bi system, shown in the upper panel. The lower panel presents the formation enthalpies of a subset of local minima with ΔH_{ch} values below 35 meV/atom. (b) Formation enthalpies calculated using DFT for the subset of structures shown in the lower panel of (a). These structures were fully optimized using DFT.

D. Density of states computed using different PAW potentials

We performed single-point DFT calculations to obtain the density of states (DOS) for some global minimum structures of the Eu–Bi and Gd–Bi systems, using PAW potentials different from those employed in the main text. In these PAW potentials, $4f$ and $5s$ electrons are regarded as valence states in Eu and Gd. The configurations of the valence electrons in the PAW potentials are $4f^7 5s^2 5p^6 6s^2$ for Eu, $4f^7 5s^2 5p^6 5d^1 6s^2$ for Gd. Spin-polarized DFT calculations were carried out using the plane-wave-basis PAW method [17, 18] within the Perdew–Burke–Ernzerhof exchange-correlation functional [19] as implemented in the VASP code [20–22]. The cutoff energy was set to 500 eV. Strong on-site electron correlations were treated using the DFT+U approach [23], assuming a ferromagnetic alignment of the magnetic moments. The Coulomb and exchange parameters, U and J, were set to 7.0 and 0.75 eV, respectively [24, 25], for the Eu and Gd $4f$ orbitals. The total energies were converged to less than 10^{-3} meV per cell. To obtain accurate DOS, we use a finer k-point grid spacing of approximately 0.06 Å^{-1}. The atomic positions and lattice constants of these structures were optimized until the residual forces were less than 10^{-2} eV/Å. These PAW potentials include scalar-relativistic corrections, and spin-orbit coupling was not explicitly considered in these systems.

Figure 21 shows the DOS for Cu_3Au-type Eu_3Bi, CuAu-type EuBi, and Cu_3Au-type $EuBi_3$ at 0 and 20 GPa, calculated using two types of PAW potentials for Eu. For $EuBi_3$ and EuBi, the DOS below the Fermi energy, calculated using a PAW potential in which the Eu $4f$ and $5s$ electrons are treated as core states, is consistent with that obtained using a PAW potential treating these electrons as valence states at both pressures. In contrast, for the Eu-rich composition Eu_3Bi, the DOS calculated with the two types of PAW potentials shows differences at both pressures, mainly due to discrepancies in the Eu p and d projected states. For Cu_3Au-type $EuBi_3$, treating the f-electrons as valence states slightly increases the optimized lattice parameter a at 0 GPa, from 5.01 Å to 5.05 Å. In contrast, for Cu_3Au-type Eu_3Bi, the effect is more pronounced, with the lattice parameter changing from 5.16 Å to 5.31 Å.

Figure 22 shows the DOS for Cu_3Au-type Gd_3Bi and NaCl-type GdBi at 0 and 20 GPa, calculated using two types of PAW potentials for Gd. For GdBi, the DOS below the Fermi energy, calculated using a PAW potential in which the Gd $4f$ and $5s$ electrons are treated as core states, is very close to that obtained using a PAW potential treating these electrons as valence states at both pressures. For the Gd-rich Gd_3Bi, differences in the DOS below the Fermi

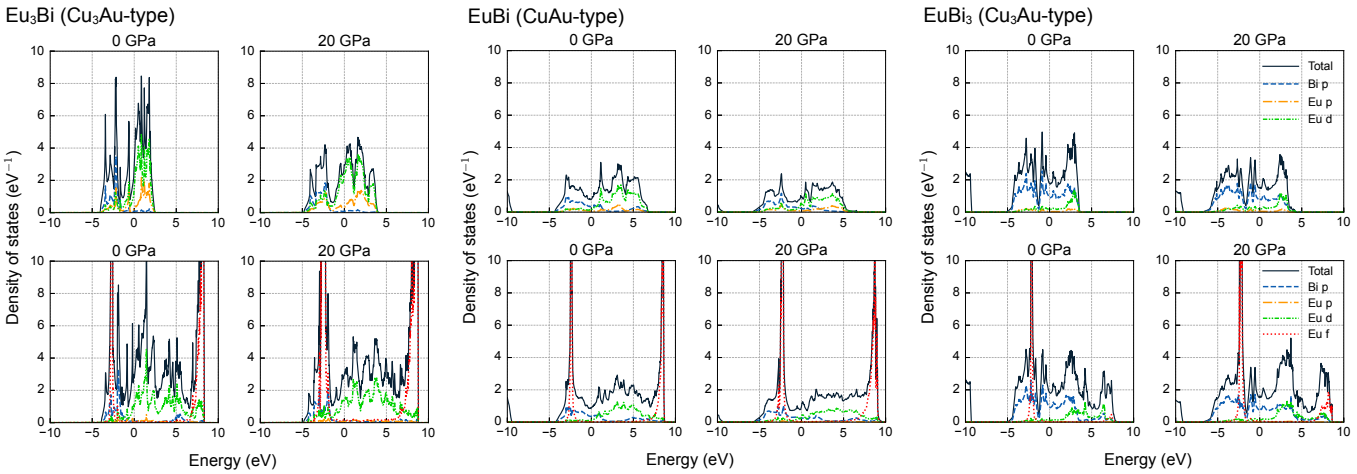

FIG. 21. DOS calculated using two types of PAW potentials, which differ in whether the Eu $4f$ and $5s$ electrons are included as valence states, for the Cu_3Au-type structures of Eu_3Bi and $EuBi_3$ and the CuAu-type structure of EuBi at 0 and 20 GPa. The top and bottom panels present the DOS obtained with PAW potentials in which the Eu valence configurations are $5p^6 6s^2$ and $4f^7 5s^2 5p^6 6s^2$, respectively. The horizontal energy axis is referenced to the Fermi energy, which is set to zero. The black line represents the total DOS, while the blue and green dashed lines and the red dotted line represent the orbital-projected DOS for Bi p, Eu p, and Eu f states, respectively.

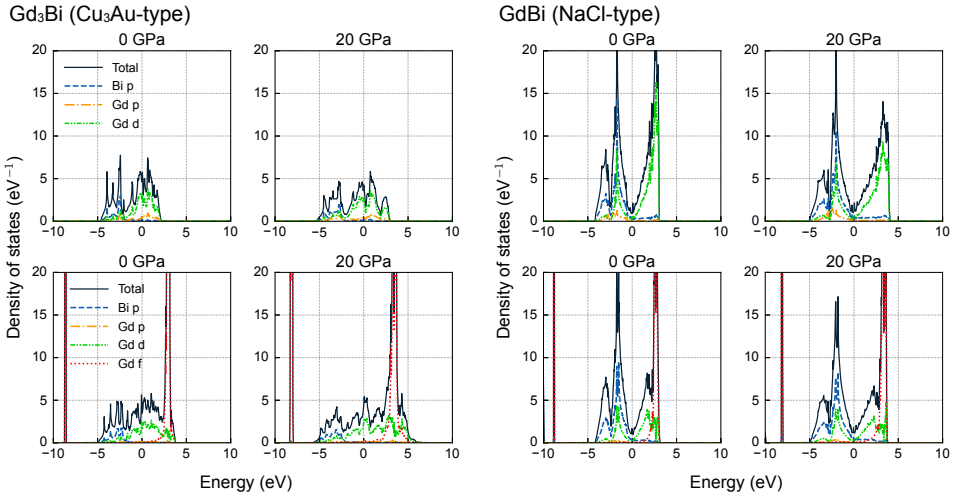

FIG. 22. DOS calculated using two types of PAW potentials for the Cu_3Au-type structures of Gd_3Bi and the NaCl-type structure of GdBi at 0 and 20 GPa. The top and bottom panels present the DOS obtained with PAW potentials in which the Gd valence configurations are $5p^6 5d^1 6s^2$ and $4f^7 5s^2 5p^6 5d^1 6s^2$, respectively. The horizontal energy axis is referenced to the Fermi energy, which is set to zero. The black line represents the total DOS, while the blue and green dashed lines and the red dotted line represent the orbital-projected DOS for Bi p, Gd p, and Gd f states, respectively.

energy computed with the two PAW potentials are also small at both 0 and 20 GPa. Treating the f-electrons as valence states slightly alters the optimized lattice parameter a at 0 GPa for both structures: from 6.38 Å to 6.39 Å for NaCl-type GdBi, and from 4.90 Å to 4.95 Å for Cu_3Au-type Gd_3Bi.

The difference in the DOS for Cu_3Au-type Eu_3Bi indicates that the f-electron effects are relatively large in Eu- and Gd-rich compositions. However, in this study, PAW potentials treating the $4f$ and $5s$ electrons as core states are employed to construct the DFT dataset and to perform DFT geometry optimizations, due to the high computational cost associated with including these electrons. Nevertheless, for the Eu- and Gd-rich compositions, the current search is able to reconstruct many experimentally reported structures, including the $Ho_{11}Ge_{10}$-type structure of $Eu_{11}Bi_{10}$, the Th_3P_4-type structures of Eu_4Bi_3 and Gd_4Bi_3, and the Mn_5Si_3-type structures of Eu_5Bi_3 and Gd_5Bi_3, indicating

that this approximation remains reasonable.

[1] O. Degtyareva, Crystal structure of simple metals at high pressures, High Press. Res. **30**, 343 (2010).
[2] E. Y. Tonkov and E. Ponyatovsky, *Phase Transformations of Elements under High Pressure* (CRC press, 2018).
[3] H. Fujihisa, Y. Akahama, H. Kawamura, Y. Gotoh, H. Yamawaki, M. Sakashita, S. Takeya, and K. Honda, Incommensurate composite crystal structure of scandium-ii, Phys. Rev. B **72**, 132103 (2005).
[4] S.-C. Zhu, X.-Z. Yan, S. Fredericks, Y.-L. Li, and Q. Zhu, First-principles investigation of Sc-III/IV under high pressure, Phys. Rev. B **98**, 214116 (2018).
[5] V. G. Tissen, E. G. Ponyatovskii, M. V. Nefedova, F. Porsch, and W. B. Holzapfel, Effect of pressure on the superconducting T_c of lanthanum, Phys. Rev. B **53**, 8238 (1996).
[6] W. Chen, D. V. Semenok, I. A. Troyan, A. G. Ivanova, X. Huang, A. R. Oganov, and T. Cui, Superconductivity and equation of state of lanthanum at megabar pressures, Phys. Rev. B **102**, 134510 (2020).
[7] W. Bi, Y. Meng, R. S. Kumar, A. L. Cornelius, W. W. Tipton, R. G. Hennig, Y. Zhang, C. Chen, and J. S. Schilling, Pressure-induced structural transitions in europium to 92 GPa, Phys. Rev. B **83**, 104106 (2011).
[8] R. J. Husband, I. Loa, G. W. Stinton, S. R. Evans, G. J. Ackland, and M. I. McMahon, Europium-IV: An Incommensurately Modulated Crystal Structure in the Lanthanides, Phys. Rev. Lett. **109**, 095503 (2012).
[9] J. Akella, G. S. Smith, and A. P. Jephcoat, High-pressure phase transformation studies in gadolinium to 106 GPa, J. Phys. Chem. Solids **49**, 573 (1988).
[10] D. Errandonea, R. Boehler, B. Schwager, and M. Mezouar, Structural studies of gadolinium at high pressure and temperature, Phys. Rev. B **75**, 014103 (2007).
[11] K. Momma and F. Izumi, *VESTA3* for three-dimensional visualization of crystal, volumetric and morphology data, J. Appl. Crystallogr. **44**, 1272 (2011).
[12] M. I. McMahon, O. Degtyareva, and R. J. Nelmes, Ba-IV-Type Incommensurate Crystal Structure in Group-V Metals, Phys. Rev. Lett. **85**, 4896 (2000).
[13] O. Degtyareva, M. I. MCMahon, and R. J. Nelmes, High-pressure structural studies of group-15 elements, High Press. Res. **24**, 319 (2004).
[14] R. J. Husband, E. F. O'Bannon, H.-P. Liermann, M. J. Lipp, A. S. J. Méndez, Z. Konôpková, E. E. McBride, W. J. Evans, and Z. Jenei, Compression-rate dependence of pressure-induced phase transitions in bi, Sci. Rep. **11**, 14859 (2021).
[15] U. Häussermann, K. Söderberg, and R. Norrestam, Comparative Study of the High-Pressure Behavior of As, Sb, and Bi, J. Am. Chem. Soc. **124**, 15359 (2002).
[16] A. Seko, Globally stable and metastable crystal structure enumeration using polynomial machine learning potentials for elemental As, Bi, Ga, In, La, P, Sb, Sn, and Te, Phys. Rev. B **110**, 224102 (2024).
[17] P. E. Blöchl, Projector augmented-wave method, Phys. Rev. B **50**, 17953 (1994).
[18] G. Kresse and D. Joubert, From ultrasoft pseudopotentials to the projector augmented-wave method, Phys. Rev. B **59**, 1758 (1999).
[19] J. P. Perdew, K. Burke, and M. Ernzerhof, Generalized Gradient Approximation Made Simple, Phys. Rev. Lett. **77**, 3865 (1996).
[20] G. Kresse and J. Hafner, Ab initio molecular dynamics for liquid metals, Phys. Rev. B **47**, 558 (1993).
[21] G. Kresse and J. Furthmüller, Efficient iterative schemes for ab initio total-energy calculations using a plane-wave basis set, Phys. Rev. B **54**, 11169 (1996).
[22] G. Kresse and J. Furthmüller, Efficiency of ab-initio total energy calculations for metals and semiconductors using a plane-wave basis set, Comput. Mater. Sci. **6**, 15 (1996).
[23] A. I. Liechtenstein, V. I. Anisimov, and J. Zaanen, Density-functional theory and strong interactions: Orbital ordering in Mott-Hubbard insulators, Phys. Rev. B **52**, R5467 (1995).
[24] J. Kuneš and R. Laskowski, Magnetic ground state and Fermi surface of bcc Eu, Phys. Rev. B **70**, 174415 (2004).
[25] G. Concas, J. K. Dewhurst, A. Sanna, S. Sharma, and S. Massidda, Anisotropic exchange interaction between nonmagnetic europium cations in Eu_2O_3, Phys. Rev. B **84**, 014427 (2011).